GLOBMAP SWF: a global annual surface water cover frequency dataset during 2000-2020 ~~for change analysis of inland water bodies~~

Yang Liu[1], Ronggao Liu[1], Rong Shang[2]

[1]State Key Laboratory of Resources and Environmental Information System, Institute of Geographic Sciences and Natural Resources Research, CAS, Beijing, 100101, China
[2]Key Laboratory for Humid Subtropical Eco-geographical Process of the Ministry of Education, School of Geographical Sciences, Fujian Normal University, Fuzhou, 350007, China

Correspondence to: Ronggao Liu (liurg@igsnrr.ac.cn)

Abstract. The extent of surface water has been changing significantly due to climatic change and human activities. However, it is challenging to capture the interannual changes of inland water bodies due to their high seasonal variation and abrupt change. In this paper, a global annual surface water cover frequency dataset (GLOBMAP SWF) was generated from the MODIS land surface reflectance products during 2000-2020 to describe the seasonal and interannual dynamics of surface water. Surface water cover frequency (SWF) was proposed as the percentage of the time period when a pixel is covered by water in a year. Instead of determination of the water directly, the SWF was estimated indirectly by identifying land observations among annual clear-sky observations to reduce the influence of clouds and variability of water bodies and surface background characteristics, which helps to improve the applicability of the algorithm for different regions across the globe. ~~Regional analysis demonstrates that our estimation results~~ The generated dataset shows better performances on frozen water, saline lake, bright surface and cloud-frequent regions compared with the two high-frequent surface water datasets derived from MODIS data, and it captures more intermittent surface water but may underestimate small water bodies when compared with two high-resolution datasets derived from Landsat data. Compared with the high-resolution SWF maps extracted from Sentinel-1 data in ~~four~~ eight regions that cover lake, river and wetland, the R^2 reaches 0.~~46~~83 to 0.97, RMSE is ranging from 7.24% to ~~11.28~~22.62%, and MAE is between 2.07% and 7.15%. In 2020, the area of global maximum surface water extent is 3.38 million km^2, of which the permanent surface water accounts for approximately 54% (1.83 million km^2) and the other 46% is intermittent surface water (1.55 million km^2). The area of global maximum and permanent surface water has been shrinking since 2001, with a change rate of -7577 km^2/yr and -4315 km^2/yr ($p < 0.05$), respectively; while the intermittent surface water with the SWF above 50% has been expanding (1368 km^2/yr, $p < 0.01$). This dataset can be used to analyze the interannual variation and change trend of highly dynamic inland waters extent with consideration of its seasonal variation. The GLOBMAP SWF data are available at https://doi.org/10.5281/zenodo.6462883 (Liu and Liu, 2022).

1 Introduction

Surface water, comprised of natural lakes, rivers, reservoirs and seasonally flooded waters, supplies water resources for maintenance of the functions of terrestrial ecosystem and livelihoods of human society. It plays a vital role in global hydrological cycle, carbon cycle and climate system (Karlsson et al., 2021), and also provides habitats for aquatic animals and plants. Inland waters usually show significant interannual and seasonal variations due to seasonality and changes of precipitation and evaporation as well as human activities (Konapala et al., 2020). The extent of surface water is suggested to be a sensitive indicator of climatic change and also responds to human activities (Zhang et al., 2019). And their changes impact global hydrological and carbon cycles and the availability of water resources, which would affect human society and ecosystems sustainability (Padron et al., 2020; Miara et al., 2017; Ran et al., 2021).

Surface water has been monitored using satellite repeated observations of the Earth's surface. The extent of inland water bodies has been mapped with active and passive microwaves observations, which can penetrate clouds and vegetation to a certain extent. Several global surface water datasets have been generated from microwaves observations, and provide monthly or weekly water cover maps at a spatial resolution of dozens of kilometers. For example, the Global Inundation Extent from Multi-Satellites datasets (GIEMS) were created by fusing multiple satellite observations of passive and active microwaves along with visible and near-infrared imagery, which describe the monthly distribution of global surface water extent at 0.25° resolution (Prigent et al., 2007; Papa et al., 2010; Prigent et al., 2020). A weekly inland water fraction dataset (Global-SWAF) was produced at a spatial resolution of 25 km based on L-band multi-angle and dual polarization microwave satellite data from the Soil Moisture Ocean Salinity (SMOS) mission over the period of 2010 to 2019 (Al Bitar et al., 2020). In recent years, with the availability of the Sentinel-1 C-band Synthetic Aperture Radar (SAR) data, a few regional 10 m-resolution water body datasets have been developed, such as High Spatial-Temporal Water Body dataset in China (HSWDC) during 2016-2018 (Li et al., 2020). But these high-resolution datasets can only cover the period since the launch of Sentinel-1.

Surface water was also ~~mapping~~ mapped with optical satellite data, which can provide long-term observations of the Earth's surface at tens to hundreds of meters resolution. Several global 30 m-resolution surface water datasets have been generated from optical high-resolution satellite data, such as Landsat (e.g., Liao et al., 2014; Pekel et al., 2016; Feng et al., 2016; Pickens et al., 2020). These datasets can describe the detailed spatial distribution of inland water bodies, usually the maximum surface water extent during the observing period. Surface water generally shows remarkable seasonal and interannual variations, and may fluctuate abruptly during a short period due to rainfall or reservoir constructions (Berghuijs et al., 2014; Lutz et al., 2014; Pickens et al., 2020). The approaches based on high spatial-resolution optical images only provide limited number of the snapshots of water cover and their averaged change rate of area over a specific period of several years. The sparse temporal sampling of these satellites makes it difficult for them to capture interannual and seasonal variations of inland waters, even misrepresented by the abrupt fluctuation of water cover.

The Moderate Resolution Imaging Spectroradiometer (MODIS) carried on the Terra and Aqua satellites with its daily revisiting period, provides a powerful tool to capture the dynamics of surface water. Several global and regional high-frequent surface water products have been generated using MODIS data. Daily global datasets of inland water bodies were generated at 250-500 m resolution (Klein et al., 2017; Ji et al., 2018), and 8-day datasets were also created at 250 m resolution at global (Han and Niu, 2020) and regional (Lu et al., 2019) scales. Several datasets for reservoirs and large lakes were also produced from MODIS observations at 8-day temporal and 250-500 m spatial resolution (Khandelwal et al., 2017; Tortini et al., 2020; Li et al., 2021). These high-frequent datasets generally directly identify water pixels for each daily or multi-day composite satellite scene using the following steps. The satellite observation is usually preprocessed to exclude the effects of cloud, ice/snow and shadow. Then, the water pixels are identified for clear-sky observations using threshold or classification methods based on reflectance on the visible, near-infrared (NIR), short-wave infrared (SWIR) bands and spectral indices. Finally, the missing data from clouds and other contaminations are usually filled using temporal interpolation to generate a gap-free time series of inland waters. The high-frequent datasets can capture the seasonal variation and short-term fluctuation of surface water extent with their daily or 8-day time series maps. However, since the timing of precipitation and human activity (such as reservoir impoundment and drainage) may shift among years, it would be incomparable for the snapshot of surface water even acquired on the same day of the year (DOY), which would conceal the real change trend when directly using these high-frequent datasets. Additionally, clouds and variable characteristics of water body and surface background may affect the performance of water mapping algorithm, making it challenging to accurately extract surface water cover at a global scale. For example, special water bodies, such as frozen water and saline lakes, may show different spectral characteristics compared with that of pure water and reduce the applicability of the algorithm; and it is difficult to accurately identify all clouds, snow/ice pixels, which would introduce uncertainties to the estimation results.

In this paper, a global annual surface water cover frequency dataset (GLOBMAP SWF) was generated from MODIS land surface reflectance data with a resolution of 500 m from 2000 to 2020. The seasonal variation of surface water was simplified to the percentage of the time period when a pixel is covered by water in a year (surface water cover frequency, SWF) to characterize the seasonal and interannual dynamics of surface water. The SWF transforms a discrete variable (water or land) into a continuous variable that can describe the distribution and life cycle of intermittent surface water. It can help to avoid the interannual mismatch issue mentioned above by excluding the influence of different occurrence periods of water cover. The SWF was estimated from MODIS observations annually. The estimation results were compared with two high-frequent surface water products derived from MODIS and two high-spatial resolution products derived from Landsat, and validated with the SWF maps derived from Sentinel-1 SAR data. Several examples were also provided to demonstrate its application for the characterization of seasonal and interannual dynamics of inland water bodies.

2 Datasets

2.1 MODIS land surface reflectance products for surface water extraction

The MOD09A1 land surface reflectance product (Version 6) (https://search.earthdata.nasa.gov/, last access: 20 November 2021) was used to generate the SWF dataset. This product contains the atmospherically corrected surface spectral reflectance of MODIS 1-7 bands, including three visible bands (red, blue, green), one NIR bands and three SWIR bands (1.2, 1.6 and 2.1 μm) (Vermote, 2015). The 8-day composited surface reflectance with low view angle and absence of clouds or cloud shadows and aerosol loading if available are provided at 500-m resolution in the Sinusoidal projection. The red, NIR and SWIR bands are sensitive to the boundaries and properties of water, land, cloud and aerosols. Here, the reflectance of MODIS Band 1 (red, 0.620-0.670 μm), Band 2 (NIR, 0.841-0.876 μm) and Band 7 (SWIR, 2.105-2.155 μm) bands were utilized to estimate the SWF. Among them, the red and SWIR bands were used to determineate land observations, and the NIR band was used to extract the annual maximum surface water extent and distinguish water from cloud and ice/snow.

2.2 Digital elevation model for mountain shadow exclusion

The digital elevation model (DEM) of the U. S. Geological Survey (USGS) Global 30 Arc-Second Elevation (GTOPO30) (https://earthexplorer.usgs.gov/, last access: 20 October 2021) was used to exclude mountain shadow in the extraction of the annual maximum surface water extent. This product provides DEM of the entire Earth's surface with geographic coordinate and horizontal datum of WGS84 in a resolution of 30 arc-seconds (approximately 900 m). The elevation data was derived from eight sources of topographic information, including Digital Terrain Elevation Data, Digital Chart of the World, USGS 1-degree DEM's, Army Map Service 1:1,000,000-scale maps, International Map of the World 1:1,000,000-scale maps, Peru 1:1,000,000-scale map, New Zealand DEM and Antarctic Digital Database. The elevation data were transferred to the Sinusoidal projection to be consistent with that of MODIS land surface reflectance data, and used to calculate the terrain slope for mountain shadow exclusion.

2.3 Surface water datasets for comparison

Two high-frequent surface water datasets derived from MODIS data and two high-resolution datasets derived from Landsat data were employed for comparison purposes, including the global surface water change database from Ji et al. (2018) (hereafter referred to as GSWCD) and Inland Surface Water Dataset in China (ISWDC) (Lu et al., 2019), Global Surface Water dataset (GSW) from Pekel et al. (2016) and the global inland water dataset derived by the Global Land Analysis and Discovery laboratory (hereafter referred to as GLAD) (Pickens et al., 2020).

The GSWCD provides global daily water maps at 500 m resolution during 2001-2016 derived from the MODIS daily reflectance time series (http://data.ess.tsinghua.edu.cn/modis_500_2001_2016_waterbody.html, last access: 12 January 2022). The cloud, ice/snow and no valid data were labeled with MODIS State QA layer and land surface temperature data. Water was identified on each single-date reflectance image with the assumption that reflectance of water at the visible bands

should be higher than at the SWIR bands, as well as thresholds of reflectance in visible and SWIR bands. For those pixels with low reflectance in visible bands, the spectral property assumption may not be exhibited, thresholds of visible and SWIR bands reflectance were used to identify water pixels, and normalized difference vegetation index (NDVI) was used to reduce the confusion between water and dense vegetation. The shadow effects caused by mountains and clouds were reduced with terrain slope derived from ASTER DEM data and cloud shadow flag of MODIS State QA layer, respectively. The cloud, ice/snow and no valid data were labeled with MODIS State QA layer and land surface temperature data, and Cloud and no valid data were filled with temporal-spatial interpolation to produce a gap-free time series. The producer's accuracy and user's accuracy of the GSWCD product were reported better than 90% when compared with classification results derived from Landsat images and manually interpreted samples.

The ISWDC product maps water bodies larger than 0.0625 km^2 within the land mass of China for the period 2000-2016 with 8-day temporal and 250 m spatial resolution (https://zenodo.org/record/2616035, last access: 12 January 2022). The surface water boundary was extracted based on the modified Otsu threshold method with reflectance of MODIS NIR band. The threshold value were was determined for four seasons with 423 selected samples of lakes and rivers. The interferences wereas removed with terrain slope derived from SRTM DEM data. The producer's accuracy and user's accuracy of the ISWDC product were reported of 88.95% and 91.13% when compared with samples from lakes and rivers derived from the China national 30 m land cover dataset (Liu et al., 2014).

The GSW product provides global surface water maps for the period 1984-2020 with 30 m resolution (https://global-surface-water.appspot.com/download, last access: 10 August 2022). The pixels in Landsat 5, 7, and 8 data were classified as open water, land or non-valid observation using the combination of expert systems, visual analytics and evidential reasoning. The classifier produces less than 1% of false water detections and misses less than 5% of water when measured using over 40,000 reference points. A seasonality dataset is contained in the GSW products to describe the intra-annual distribution of water and used to compare with our estimation results. A permanent water surface is underwater throughout 12 months of the year (with the seasonality value of 12), while a seasonal water surface is with the value less than 12. For lakes freeze for part of the year, the dataset treats ice as a non-valid observation, and the observation period corresponds only to the unfrozen months.

The GLAD product maps global inland water for the period 1999-2020 with 30 m resolution (https://www.glad.umd.edu/dataset/global-surface-water-dynamics, last access: 10 August 2022). The land and water were classified in all Landsat 5, 7, and 8 scenes and performed a time-series analysis to produce maps that characterize inter-annual and intra-annual open surface water dynamics. Each Landsat scene was classified into land, water, cloud, shadow, haze and snow/ice with ensembles of classification trees. The producer's accuracy and user's accuracy of the GLAD monthly mapped water class were reported of 96.0% and 93.7% when compared with reference sample data. Annual water percent dataset is contained in the GLAD products to characterize the seasonality of the water cover and used to compare with our results. The land and water observations of a given pixel were summed per month and aggregated into water presence frequency, measured by the percent of clear observations flagged as water.

2.4 Datasets for validation

The estimation results were validated with the SWF maps extracted from Sentinel-1 data. To evaluate of the performance of our dataset for different surface water types, permanent and seasonal waters, different latitudes, as well as with presence of frequent cloud cover, ~~four~~ eight regions were selected for validation, including Lake Albert in the Democratic Republic of the Congo and Uganda (30.98° E, 1.74° N), Lake Mai-Ndombe in the Democratic Republic of the Congo in southwestern part of Congo Basin (18.32° E, 2.07° S), River Amazon and River Taparus in western Amazon in Brazil (54.87° W, 2.16° S), ~~and~~ wetlands in western Bangladesh (91.12° E, 24.65° N), Lake Winnipegosis in Canada (99.91° W, 52.61° N), lakes in western Russia (31.00° E, 64.10° N), Lake Maggiore in Italy (8.65° E, 45.90° N), and Lake Wakatipu in New Zealand (168.55° E, 45.10° S). These areas cover major types of inland water bodies, including lake, river and wetland. Among them, the ~~two~~six lake~~s~~ regions and River Taparus are dominated by permanent surface water, River Amazon has seasonal water cover, and wetlands in western Bangladesh are dominated by seasonal surface water. Lake Albert, Lake Mai-Ndombe, River Amazon and River Taparus and wetlands in western Bangladesh are in the tropics and subtropics. Cloud and rain should be frequently ~~occur~~occurred in the~~se~~ four regions ~~located in the tropics and subtropics~~, especially for River Amazon (Taparus) and Lake Mai-Ndombe in the Amazon and Congo Basin respectively, which helps to evaluate the performance in frequently cloud-covered areas. Lake Maggiore and Lake Wakatipu are in the middle latitudes of the northern and southern Hemispheres, respectively. The former is surrounded by mountains in the Alps in northern Italy, which shows an example of the performance in mountainous regions. Lake Winnipegosis and lakes in western Russia are in high latitudes of the Northern Hemisphere, where concentrated a large number of small water bodies.

The Sentinel-1 mission images the entire Earth every six days with a constellation of two satellites orbiting 180˚ apart, and the repeat frequency is just three days at the equator and less than one day over the Arctic. The C-band Synthetic Aperture Radar (SAR) it carries can penetrate cloud and rain to provide an all-weather supply of imagery of the Earth's surface, which helps to accurately characterize the inundation frequency. All available vertical transmission and vertical reception (VV) polarization data of Sentinel-1A and Sentinel-1B in 2020 were used to extract the surface water extent of the ~~four~~ eight regions at 10 m resolution utilizing Google Earth Engine (GEE). A median filter method was used to reduce speckle noise in SAR images (Bioresita et al., 2018). The water pixels were identified for each available image based on the Otsu algorithm, which maps the surface water extent with an unsupervised histogram-based thresholding approach that automatically selects the optimal threshold of water and non-water by maximizing the variance between classes (Otsu, 1979). The Sentinel-1 SWF was mapped by calculating the percentage of water observations count to the total count of observations for each pixel. For regions at high and middle latitudes, the observations covered with snow and ice were excluded and the SWF was calculated with Sentinel-1 observations during the unfrozen period.

3 Methodology

3.1 Extraction of surface water cover frequency

190 Clouds and ice/snow may affect accurate detection of inland surface water based on optical remote sensing, especially for water bodies with high reflectivity. To reduce the interferences of clouds and ice/snow, this paper does not directly detect water pixels, but extract surface water through identifying land observations in annual MODIS observation series. We found high reliability distinguishing features for the separation of land, water, cloud and ice/snow. The former usually has a lower reflectivity in the visible band than in the SWIR band, while the latter three are the opposite. And the cloud and ice/snow can

195 be excluded with higher reflectance in NIR band compared to water and land. Based on these spectral characteristics, the SWF was estimated using four steps from MOD09A1 land surface reflectance data (Fig. 1), including counting the number of clear-sky land observations, determining the maximum surface water extent, estimating the total number of clear-sky observations over the maximum surface water extent, and calculating the SWF.
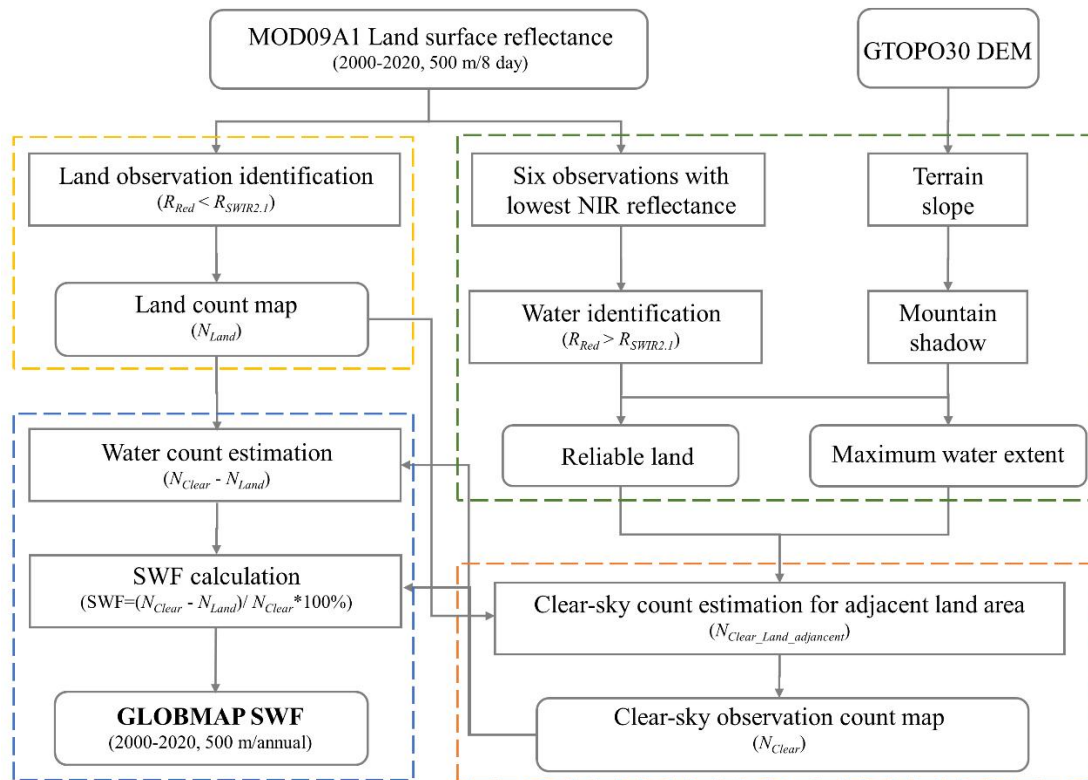
200 **Figure 1.** Workflow of the method for generating GLOBMAP surface water cover frequency dataset.

Firstly, the number of clear-sky land observations during a whole year (N_{Land}) was counted for each pixel from the MOD09A1 annual land surface reflectance series. The land observations were separated from water and cloud using the reflectance in the red band (R_{Red}) and SWIR band with wavelength of 2.1 μm ($R_{SWIR2.1}$). Those pixels with $R_{Red} < R_{SWIR2.1}$

were labeled as land. Since R_{Red} is generally higher than $R_{SWIR2.1}$ for water, cloud and snow/ice, the land observations can be reliably identified without the help of cloud masks.

Then, the annual maximum surface water extent was determined from the six observations with the lowest NIR reflectance during a specific year. Water generally has low reflectance in the NIR band (R_{NIR}), while presence of cloud and ice/snow would significantly increase the R_{NIR}. Thus, observations with the lowest R_{NIR} should be inclined to the clear-sky inundated observation, while the cloud and ice/snow pixels could be excluded reliably. Here, six observations with the lowest R_{NIR} in a year were selected by weighing available valid observations and possible noise observations, such as shadows, burned areas and occasional water cover. Here, sixThese six observations with the lowest R_{NIR} in a year were assumed to be clear-sky observations, and water observations among them were determined using the criterion of $R_{Red} > R_{SWIR2.1}$. Those pixels with water count ≤ 1 were identified as reliable land. To exclude possible residual shadows, burned areas and occasional water cover, all pixels with water count ≥ 3 were used to create the maximum surface water extent map for the specific year. The mountain shadow was excluded using the criterion that the terrain slope derived from DEM > 30º.

The number of clear-sky observations over the maximum surface water extent (N_{Clear}) was estimated from the count of clear-sky observations of its adjacent reliable land pixels. Here, clear-sky observation refers to the valid MOD09A1 observation that not covered with clouds and snow/ice. The coverage of clouds is usually similar for land and water bodies in a small area. This study assumes that the number of clear-sky observation over the water bodies (N_{Clear}) is the same with that over adjacent land areas ($N_{Clear\_Land\_adjacent}$). Here, for each pixel in the maximum surface water extent, one hundred spatial nearest reliable land pixels were selected. The count of clear-sky observations for those reliable land pixels equals to N_{Land} since all clear-sky observation should be land for reliable land pixels. Then, the $N_{Clear\_Land\_adjacent}$ was estimated by averaging the N_{Land} values for the selected one hundred nearest reliable land pixels, and the N_{Clear} was set to equal to the estimated $N_{Clear\_Land\_adjacent}$.

Finally, the number of water observations (N_{Water}) was calculated for the pixels within the range of the maximum surface water extent by subtracting the land observation count (N_{Land}) from all clear-sky observations count (N_{Clear}). And the SWF was calculated by the water count dividing all clear-sky observations count within a year (Eq. (1)). Those pixels with N_{Land} of zero should be covered by water during the whole year, and their SWF were equal to 100%. While those pixels with N_{Land} equal to N_{Clear} should be permanent land, and their SWF were equal to 0%. ForIn large inland water bodies, the adjacent reliable land pixels that used to estimate N_{Clear} over the maximum surface water extent may be far away from the water pixels, which may result in uncertainties in N_{Clear} estimation of water pixels and the SWF consequentlymay be underestimated for the permanent water due to uncertainties in MOD09 surface reflectance data and N_{Clear} estimations derived from far adjacent land areas. Here, the SWF was set to 100% for those pixels with N_{Land} less than 15 count for global largest 100 inland water bodies excluding rivers and water bodies with great seasonal variation in water extent to reduce the influences of uncertainty in N_{Clear} on SWF dataset.

$$SWF = \frac{N_{Clear} - N_{Land}}{N_{Clear}} \times 100\% \tag{1}$$

Several post-processing procedures were then implemented to the generated SWF maps. The water bodies with an area less than 2×2 pixels were removed to reduce the influence of noise. The oceans were delineated using the ocean label in the state QA flags of MOD09A1 products. The flag of MOD09A1 was used as the initial ocean flag. Those pixels detected as land by the proposed method were labeled as land, and those water pixels between the land and the ocean flagged by MOD09A1 were labeled as ocean. For water bodies that were not marked as oceans in the state flag of MOD09A1, we extended the land boundary toward the water. If the extended land boundaries meet with each other, the water bodies were labeled as inland waters; if the extended land boundaries meet the ocean pixels, the adjacent water pixels were labeled as ocean.

3.2 Validation and inter-comparison with other products

The estimation results were validated with the SWF maps extracted from Sentinel-1 SAR observations in the four regions (Sect. 2.3). The spatial distribution of our results was compared with the Sentinel-1 results. And the Sentinel-1 SWF maps were resampled to 500 m resolution by averaging the valid SWF estimations from Sentinel-1 data within the MODIS 500 m grid~~calculating the average SWF values for each 500 m grid~~, and then compared with GLOBMAP SWF maps pixel-by-pixel. The root mean standard error (RMSE), absolute mean difference (MAE) and the coefficient of determination (R^2) were estimated to evaluate the accuracy of GLOBMAP SWF maps.

The estimation results were also compared with the GSWCD and ISWDC products that derived from MODIS observations as well as GSW and GLAD products that derived from Landsat data for characterizing the seasonal variation of surface water. The surface water maps of the ~~three~~ five datasets were demonstrated in three lake regions as examples to evaluate their performance in unfrozen water, frozen water and saline lake, as well as with the presence of clouds and bright surfaces. These include Taihu Lake in eastern China (30.62° N-31.78° N, 119.66° E-120.82° E), lakes in northeastern Tibetan Plateau (34.48° N-36.10° N, 89.71° E-91.53° E) and Qarhan Salt Lake in the southern Qaidam Basin in northwestern China (36.56° N-37.24° N, 94.48° E-96.08° E).

4 Results

4.1 Distribution of global surface water cover frequency

The estimated global SWF map in 2020 is illustrated in Fig. 2a to describe the temporal coverage of inland surface water. The maximum extent, minimum extent (permanent surface water) and intermittent surface water extent are also shown in Fig. 2b-2d to characterize the different status of inland water bodies. The intermittent surface water refers to the areas covered by water for part of a year. Some lakes freeze for part of the year. Since snow and ice observations are excluded in estimation of the SWF in the proposed method, the observations in unfrozen period are used to estimate the surface water cover frequency for the year. If area is underwater for part of the observation period (i.e., the unfrozen period), it is considered to be the intermittent surface water; while if water is present throughout the unfrozen period, the water body is considered to be a permanent surface water. Considering possible uncertainty of the algorithm and quality of satellite observations, here we use

SWF ≥ 10% for identification of the maximum water extent, SWF ≥ 90% for the minimum water extent identification, and 10% ≤ SWF < 90% for intermittent water identification. For visualization, the SWF was aggregated to 10 × 10 km grids by averaging all valid SWF values in each grid.

In 2020, the area of the maximum extent of global surface water is 3.38 million km^2, of which the permanent surface water (the minimum extent) is 1.83 million km^2 and the intermittent surface water is 1.55 million km^2. About 46% of the global total surface water cover (the maximum extent) is intermittent water, which demonstrates the remarkable seasonal dynamics of inland water cover. Compared with the Global high-resolution surface water datasets of GSW (Pekel et al., 2016), GLAD (Pickens et al., 2020) and Global 3 arc-second Water Body Map (G3WBM) (Yamazaki et al., 2015) derived from multi-temporal Landsat images, our estimation results extract less permanent surface water (2.78, 2.93 and 3.25 million km^2 for GSW, GLAD and G3WBM respectively) and the maximum surface water (4.46 and 4.82 million km^2 for GSW and GLAD respectively). This may be related to the limited spatial resolution of MODIS and post-processing of the dataset, which makes GLOBMAP SWF dataset can detect inland water body larger than 1 km×1 km open to the sky, including fresh and salt water. More intermittent surface water are captured compared with the three high-resolution datasets (0.81, 0.74, and 0.49 million km^2 for GSW, GLAD and G3WBM respectively) with aid of frequent MODIS observations to separate the seasonal and permanent water bodies. The inland water bodies are widely distributed across the globe except for the deserts and permanent snow/ice covered areas. They are mainly concentrated in mid-high latitudes of the Northern Hemisphere, such as northeast of North America, northwest of Europe, north of Russia and the Tibetan Plateau. About 67% of the maximum surface water are distributed above 35° N, and this percentage reaches 79% and 54% for the permanent surface water and intermittent surface water, respectively. The permanent surface water cover are concentrated on the lakes areas, such as Great Lakes in North America, Arctic lakes, lakes in the Tibetan Plateau. The intermittent surface water are widely distributed across the globe, especially in the high latitudes of the Northern Hemisphere, which may be related to the seasonal melting of permafrost. They are also scattered in Africa, Australia, the Pacific Islands and south parts of Eurasia and North America, which may be related to the notable seasonal variations in precipitation.
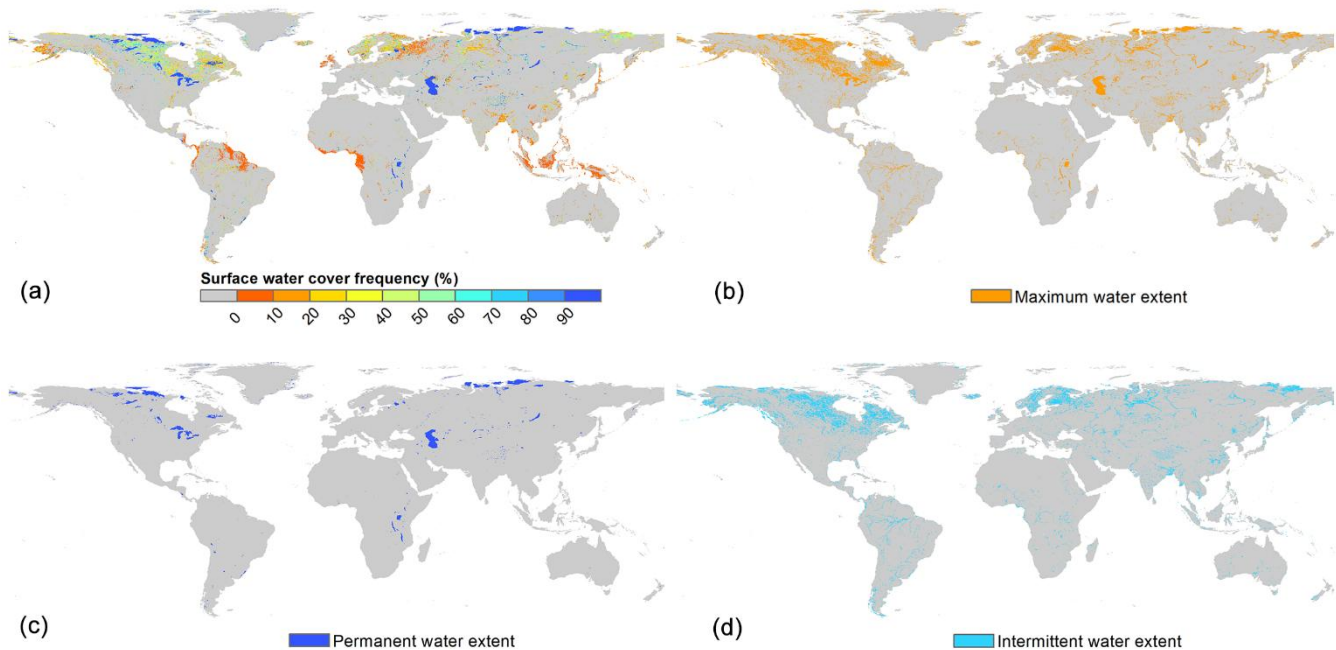
Figure 2. Global distribution of surface water cover frequency in 2020. **(a)** global SWF map; **(b)** the maximum surface water extent, **(c)** the permanent surface water extent and **(d)** the intermittent surface water extent. The SWF was aggregated to 10×10 km grids by averaging the valid SWF in each grid for visualization.

4.2 Comparison with ~~high-frequent~~existing surface water datasets

The performance of our estimates was evaluated for unfrozen water, frozen water and saline lake and compared with the ~~high-frequent~~ surface water datasets of GLAD, GSW, GSWCD and ISWDC. The effects of clouds and bright surfaces were also evaluated. The comparison was performed in three regions as examples, including Taihu Lake in eastern China, lakes in northeastern Tibetan Plateau and Qarhan Salt Lake in the southern Qaidam Basin.

The performance of unfrozen water and effects of clouds were evaluated in the Taihu Lake region, the third largest freshwater lake in China. It is located in the subtropical East Asian monsoon region, where clouds are frequently occurred in summer. Since the average water temperature of Taihu Lake in January is 4°C, water rarely freezes in winter, with only a few thin ices with a thickness of 1-2 cm in the bay or lee shore. Figure 3 shows the distribution of GLOBMAP SWF, annual water percent dataset of GLAD, seasonality dataset of GSW, and the surface water extent map of GSWCD and ISDWC products in January (DOY001) and July (DOY200) in ~~2016~~2015. Google Earth high-resolution image is presented for reference (Fig. 3a). ~~The 30 m resolution land cover maps of GlobeLand30 (Chen et al., 2015) are aggregated to 500 m by calculating the percentage of water pixels within each 500 m grid, and the water cover fraction map is also presented in Fig. 3c.~~ The results show that the spatial pattern of our estimates is in good agreement with that of the GLAD and GSW~~e water cover fraction map of GlobeLand30 and Google Earth high-resolution image~~. The GLOBMAP SWF reaches 100% in Taihu

Lake and surrounding lakes, indicating that our algorithm successfully extracts the distribution of unfrozen water and reduces the influence of clouds in this region (Fig. 3b). The two Landsat-based products capture more small lakes and narrow rivers with their fine spatial resolution, but the water occurrence of some areas in the northwest part of the Taihu Lake are underestimated, which is probably due to frequency clouds. The surface water maps of GSWCD are generally

315 consistent with our estimation results, GLAD and GSWGlobeLand30, suggesting that the interpolation algorithm of GSWCD successfully reconstructs the water cover series in this area. Many lake areas are not identified in the ISDWC maps especially for July (Fig. 3g3h), which indicates that surface water cover may be underestimated in this dataset due to clouds. Seasonal water cover is observed in our estimates with SWF lower than 30% in the south and east of Taihu Lake. These intermittent water cover may be related to the seasonal irrigation of paddy rice that are widely planted in this area.

(a) Google earth image

(b) GLOBMAP

Surface water cover frequency (%)

0 10 20 30 40 50 60 70 80 90 100

(c) GlobeLand30

Water cover fraction (%)
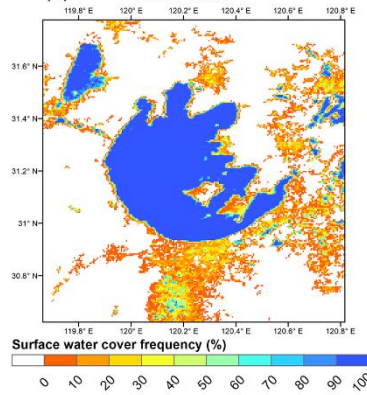
0 10 20 30 40 50 60 70 80 90 100
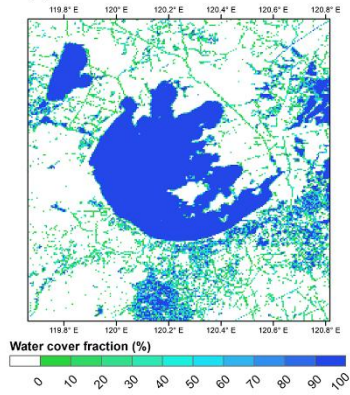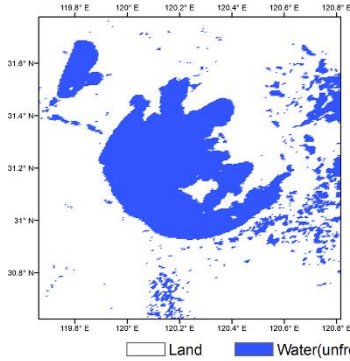
(d) GSWCD DOY001

(e) GSWCD DOY200
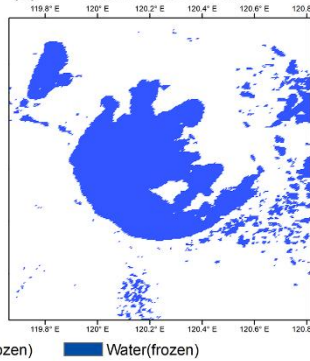
(f) ISDWC DOY001-008

(g) ISDWC DOY193-200

Land   Water(unfrozen)   Water(frozen)

Non-water   Water
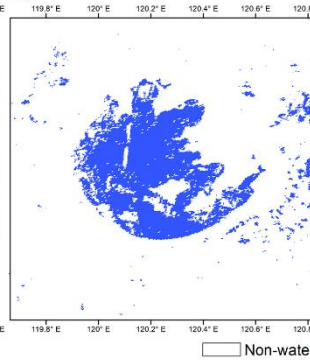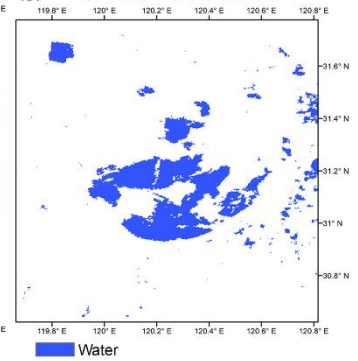
320
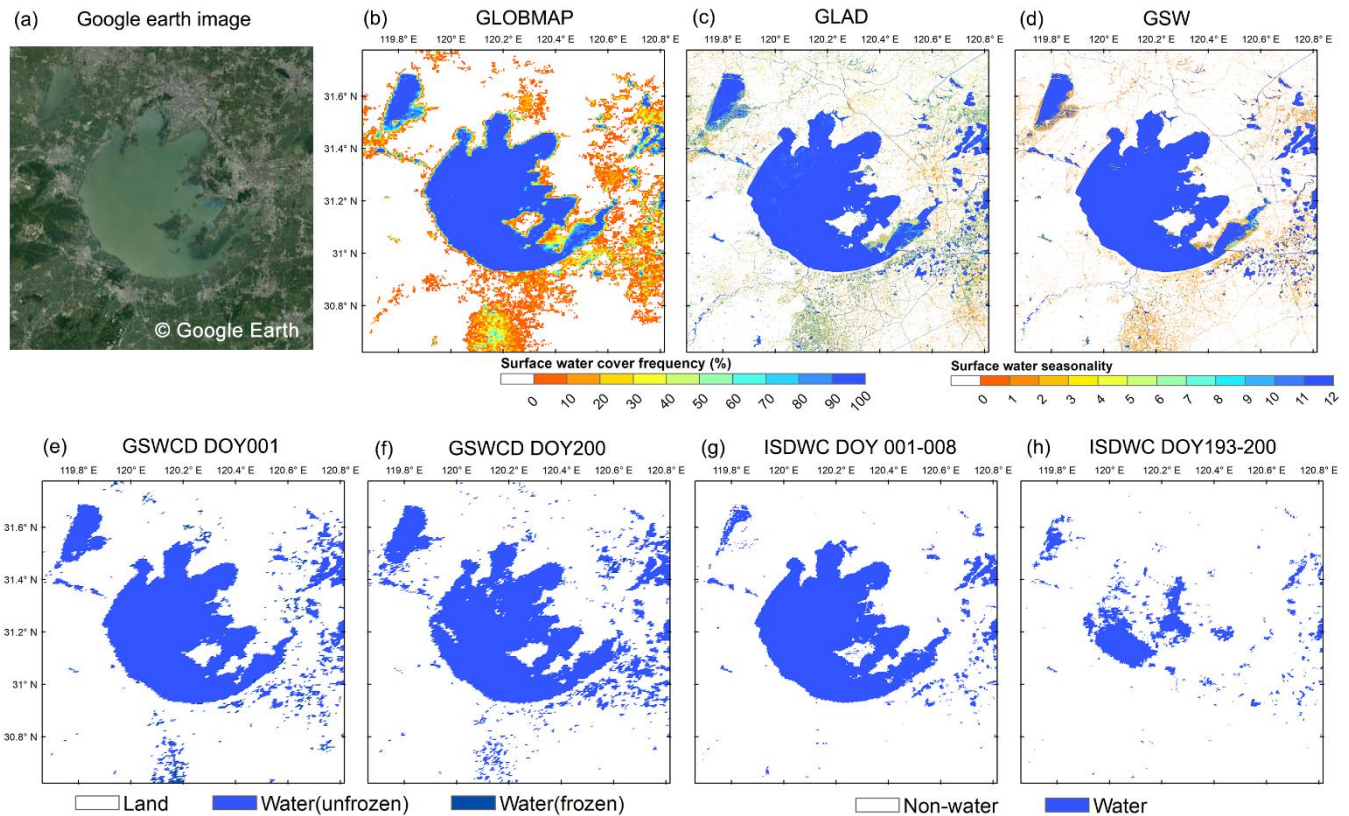
Figure 3. Comparison of surface water map of GLOBMAP SWF, ~~GLAD, GSW,~~ GSWCD and ISDWC in frequently cloud covered areas around Taihu Lake in eastern China (30.62° N-31.78° N, 119.66° E-120.82° E) in 2015. **(a)** Google Earth high-resolution image (from Google Earth); **(b)** GLOBMAP surface water cover frequency ~~in 2016~~; **(c)** ~~GlobeLand30~~ GLAD annual water percent; ~~**aggregated 500 m-**~~

325   ~~**resolution water cover fraction in 2020**~~**(d)** GSW seasonality (Source: EC JRC/Google); surface water extent of GSWCD in **(~~d~~e)** DOY001 and **(~~e~~f)** DOY200 in ~~2016~~2015; surface water extent of ISDWC in **(~~f~~g)** DOY001-008 and **(~~g~~h)** DOY193-200 in 201~~5~~6.

The performance of frozen water and impact of bright surfaces were compared in lakes in the northeast part of the Tibetan Plateau (Fig. 4). Several lakes are located in this barren area. The altitude reaches around 5000 m, and these lakes are frozen in winter due to extreme cold weather. The GLOBMAP SWF map captures the distribution of lakes in Google Earth images,

330   with the SWF reaching 100% in the lake areas (Fig. 4b). GLAD and GSW show similar spatial extent of lakes with GLOBMAP, but GLAD seems to underestimate the water occurrence in this region. The surface water cover maps of GSWCD and ISDWC products in July are consistent with our estimation results and Google Earth imagery (Fig. 4~~f~~d and 4~~h~~f). But when it comes to winter in January, some frozen water cover is undetected for the GSWCD product (red circles in Fig. 4~~e~~e), and many barren land pixels are confused with frozen water. This may be related to the similar high reflectivity in

335   the visible band and low land surface temperature for frozen water and barren land in winter. The ISDWC product fails to detect the lakes in this area in DOY001-008 in ~~2016~~ 2015 due to cloud contamination (Fig. 4~~e~~g).
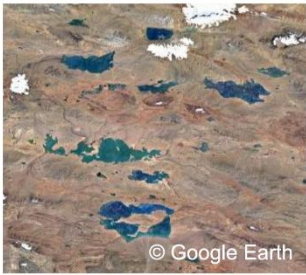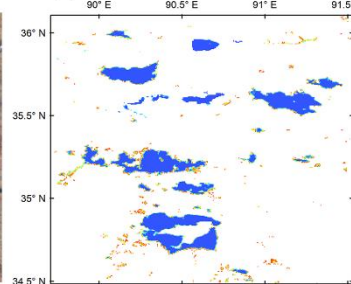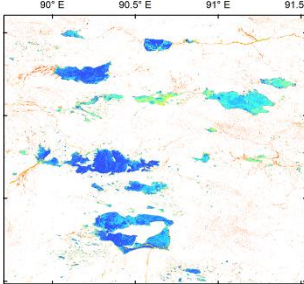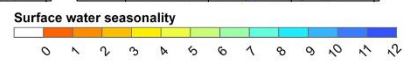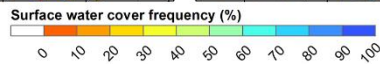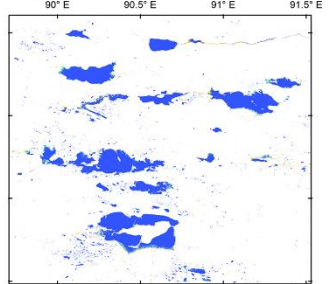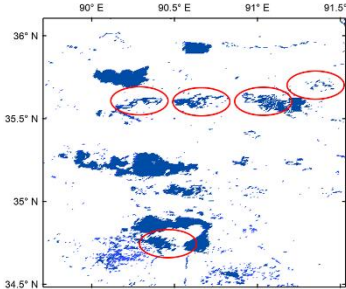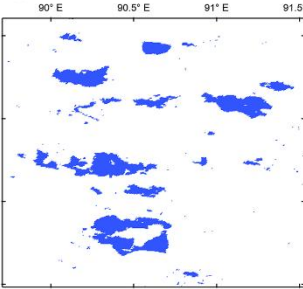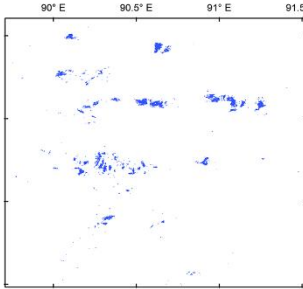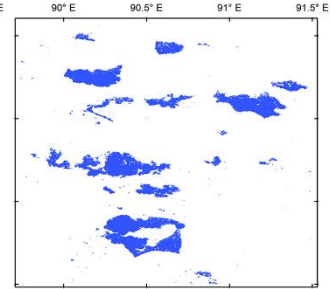
Figure 4. Comparison of surface water map of GLOBMAP SWF, GLAD, GSW, GSWCD and ISDWC for frozen lakes over bright surface in northeastern Tibetan Plateau (34.48° N-36.10° N, 89.71° E-91.53° E) in 2015. **(a)** Google Earth high-resolution image (from Google Earth); **(b)** GLOBMAP surface water cover frequency map in 2016; **(c)** GLAD annual water percent; **(d)** GSW seasonality (Source: EC JRC/Google); surface water extent of GSWCD in **(ec)** DOY001 and **(df)** DOY200 in 201~~5~~6; surface water extent of ISDWC in **(eg)** DOY001-008 and **(hf)** DOY193-200 in 201~~5~~6.

Figure 5 shows the comparison results of Qarhan Salt Lake, which is located in the Qaidam Basin on the northwestern part of the Tibetan Plateau. As the largest saline lake in China, the lake is rich in inorganic salts such as sodium chloride, potassium chloride and magnesium chloride. Corresponding to the high-resolution image of Google Earth (Fig. 5a), our estimation results, GLAD and GSW successfully extract the distribution of the saline lake. The estimated SWF is approximately 100% in the lake areas (Fig. 5b), and the derived saline lake map agrees well with the high-resolution images for the four subregions shown with the red rectangles in Fig. 5a (the third row in Fig. 5). GLAD and GSW show more spatial details of the salt lakes. The GSWCD product identifies the majority part of the lake, but some lake areas in southern and western parts are missed (red circles in Fig. ~~5d~~5f). Although clear-sky observations were obtained in this area during DOY001-008 and DOY193-200 in 2016 according to MOD09A1 data, many salty water areas are missed in the ISDWC product (red circles in Fig. ~~5e~~5g and ~~5f~~5h), indicating that the extent of saline lakes may be underestimated in this dataset. Additionally, our estimates also capture the signals of the endorheic Golmud River that flows into the southeast of the saline lake (subregion 2 in Google Earth image).
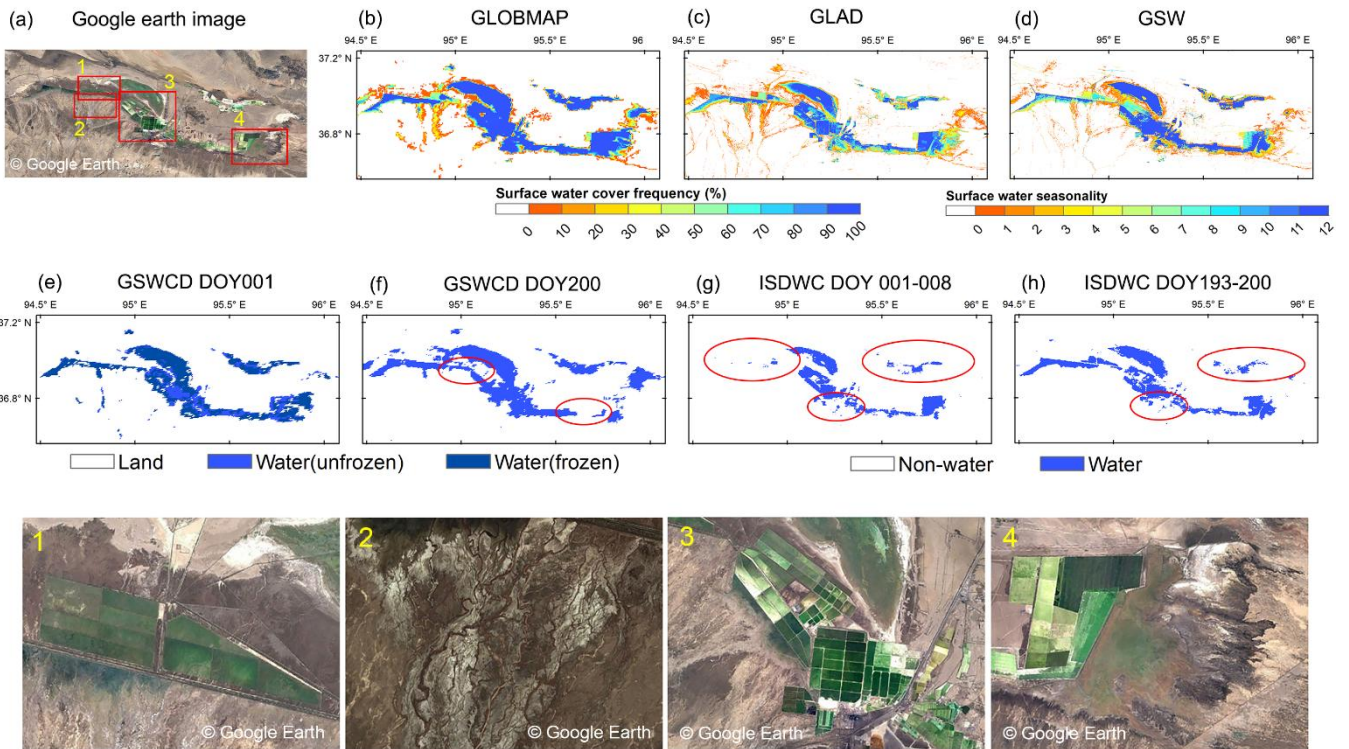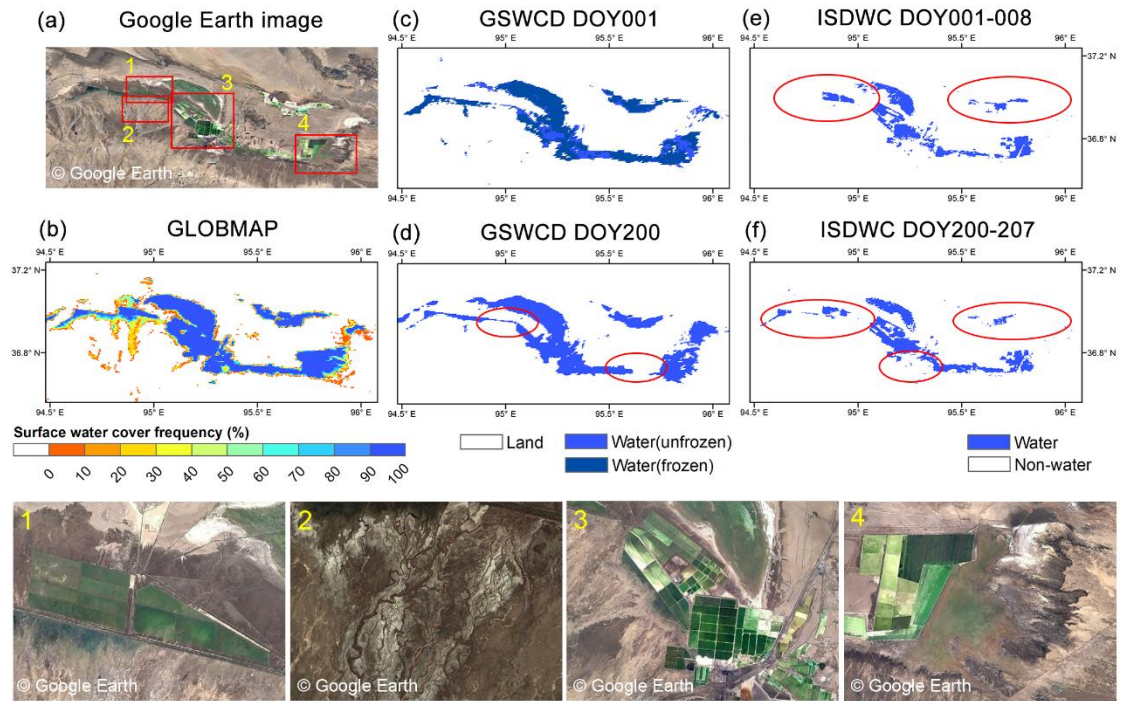
Figure 5. Comparison of surface water map of GLOBMAP SWF, GLAD, GSW, GSWCD and ISDWC for saline lake in Qarhan Salt Lake in the southern Qaidam Basin in northwestern China (36.56° N-37.24° N, 94.48° E-96.08° E) in 2015. **(a)** Google Earth high-resolution image (from Google Earth); **(b)** GLOBMAP surface water cover frequency in 2016; **(c)** GLAD annual water percent; **(d)** GSW seasonality (Source: EC JRC/Google); surface water extent of GSWCD in **(ec)** DOY001 and **(df)** DOY200 in 201~~5~~6; surface water extent of ISDWC in **(eg)** DOY001-008 and **(fh)** DOY193-200 in ~~2016~~2015. The last row shows the Google Earth high-resolution images for the four subregions shown with the red circles in Fig. 6a (from Google Earth).

4.3 Validation

The accuracy of GLOBMAP SWF dataset was assessed with the 10 m-resolution SWF maps extracted from Sentinel-1 SAR data in ~~four~~ eight regions that cover lake, river and wetland. Figure 6 presents the SWF maps of our results and Sentinel-1 as well as the linear regression results of the two datasets.

The surface water extent of GLOMAP SWF are generally consistent with that of Sentinel-1 in these regions, while Sentinel-1 SWF describes more small~~finely~~ water bodies and narrow rivers with its high spatial resolution observations. Good positive correlation is observed for SWF maps between our estimates and Sentinel-1 results, with R^2 up to above 0.75 for most regions except for lakes in western Russia (0.46)~~up to 0.83-0.97~~. For the lakes that are mainly covered by permanent surface water in the middle and low latitudes without frequent cloud covers, such as the Lake Albert in the Democratic Republic of the Congo and Uganda, Lake Maggiore in Italy and Lake Wakatipu in New Zealand, ~~that mainly covered by permanent surface water~~, the SWF maps of GLOBMAP and Sentinel-1 agree well~~best among the four regions~~, with the RMSE ranging from 7.24% to 13.20% and MAE from 2.07% to 2.45%. ~~R^2 (0.97) reaching the highest value and RMSE (7.24%) and MAE (2.07%) reaching the lowest values.~~ For Lake Maggiore that surrounded by mountains, most of the water extent was extracted compared with the Sentinel-1 results. The performance of the dataset may be affected by frequent cloud covers in tropical regions. For the Lake Mai-Ndombe in the southwestern part of the Congo Basin, our dataset can characterize the spatial extent of the lake, but the SWF may be underestimated compared with the Sentinel-1 results, and the RMSE and MAE are increased to 11.28% and 3.80% respectively, which may be due to the lack of clear-sky observations in this tropic region. In the western Amazon, both the two SWF maps show widespread seasonal water cover in the River Amazon and permanent water cover in the River Taparus, with the RMSE and MAE of 7.93% and 2.24%, respectively. Our estimation results present scattered detection with SWF < 10% in the middle and southern parts of the image, which may also be related to the frequent occurrence of clouds and rain. For the wetland in western Bangladesh, widespread intermittent water cover and complex surface conditions make it challenging to extract the SWF. Our results generally agree well with the Sentinel-1 SWF map in this region, both showing higher inundation frequency in the northern and middle parts of the wetland than in the southern part and margins, and the RMSE and MAE are still within 10.8% and 7.2%. For lakes in high latitudes, including Lake Winnipegosis and lakes in western Russia, the dataset captures the distribution of large water bodies, but may underestimate scattered small lakes in these regions due to the coarse resolution of MODIS data, which makes the RMSE and MAE increased to 16.22%-22.62% and 6.17-7.04%, respectively. The comparison indicates that our

dataset can also provide reasonable estimates for intermittent inland water bodies, and it is more reliable for large water bodies with less seasonal water cover and clouds.
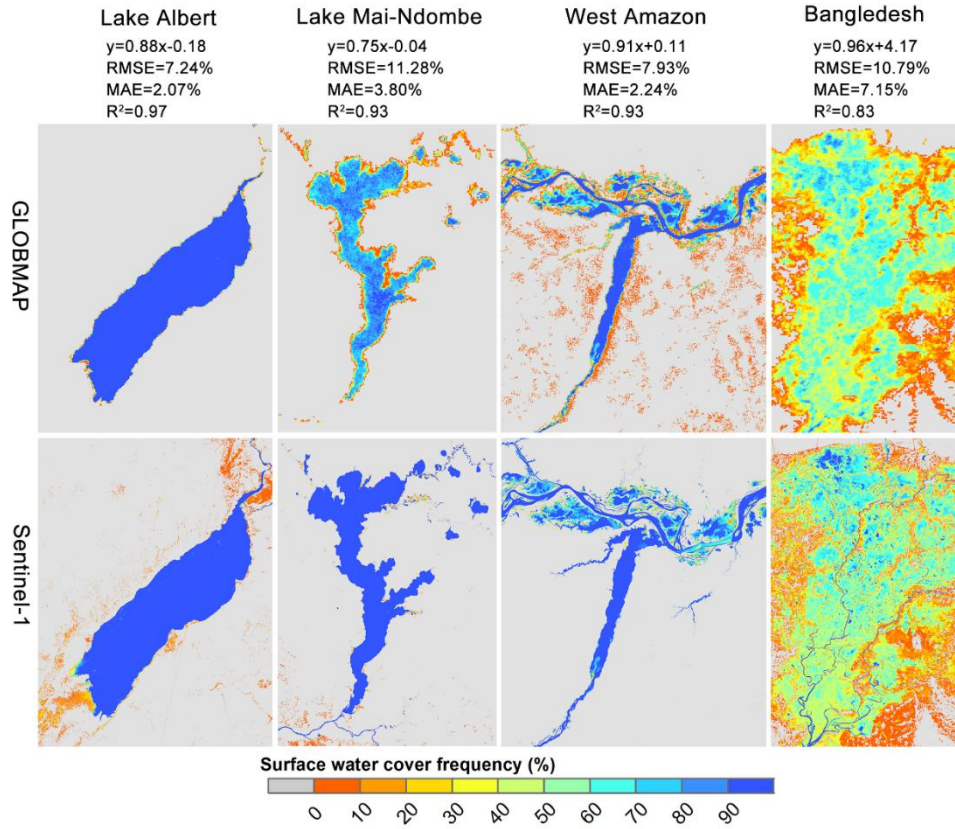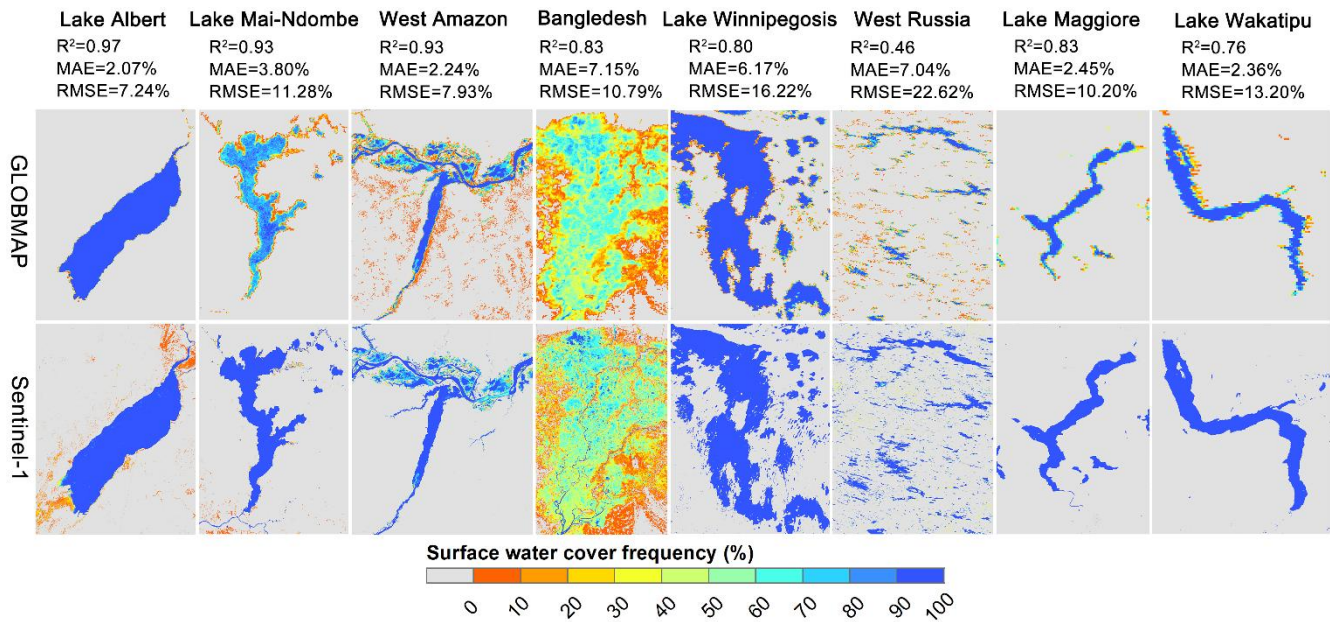
Figure 6. Comparison of GLOBMAP SWF against SWF maps derived from Sentinel-1 in ~~four~~ eight regions. These include Lake Albert in the Democratic Republic of the Congo and Uganda (30.98° E, 1.74° N), Lake Mai-Ndombe in western Democratic Republic of the Congo (18.32° E, 2.07° S), River Amazon and River Taparus in western Amazon in Brazil (54.87° W, 2.16° S), ~~and~~ wetland in western Bangladesh (91.12° E, 24.65° N), Lake Winnipegosis in Canada (99.91° W, 52.61° N), lakes in western Russia (31.00° E, 64.10° N), Lake Maggiore in Italy (8.65° E, 45.90° N), and Lake Wakatipu in New Zealand (168.55° E, 45.10° S). The linear regression results are presented in the top of the figure.

4.4 Interannual variation and change trend of global surface water

The interannual variation and change trend of global maximum, minimum and intermittent surface water were analyzed using the GLOBMAP SWF dataset from 2001 to 2020. Since the MODIS data is incomplete in 2000, the results of 2000 were not used in this analysis. Figure 7 shows interannual variation of the area of global inland water bodies with different inundation frequencies. During the past two decades, the average area of global maximum surface water (SWF $\geq$ 10%) is 3.57±0.10 million km^2, with the largest area of 3.72 million km^2 in 2008 and the smallest area of 3.38 million km^2 in 2016. The average area of the minimum surface water (permanent surface water, SWF $\geq$ 90%) is 1.89±0.03 million km^2, which is 53% of the area of maximum water extent. The permanent water reached the largest extent of 1.95 million km^2 in 2001 and the smallest extent of 1.83 km^2 in 2016. The average area of global intermittent water (10% $\leq$ SWF < 90%) is 1.68±0.08 million km^2, accounting for 47% of the maximum water area. Among them, about 79% of intermittent water occurred in less than half of a year (10%$\leq$SWF<50%).
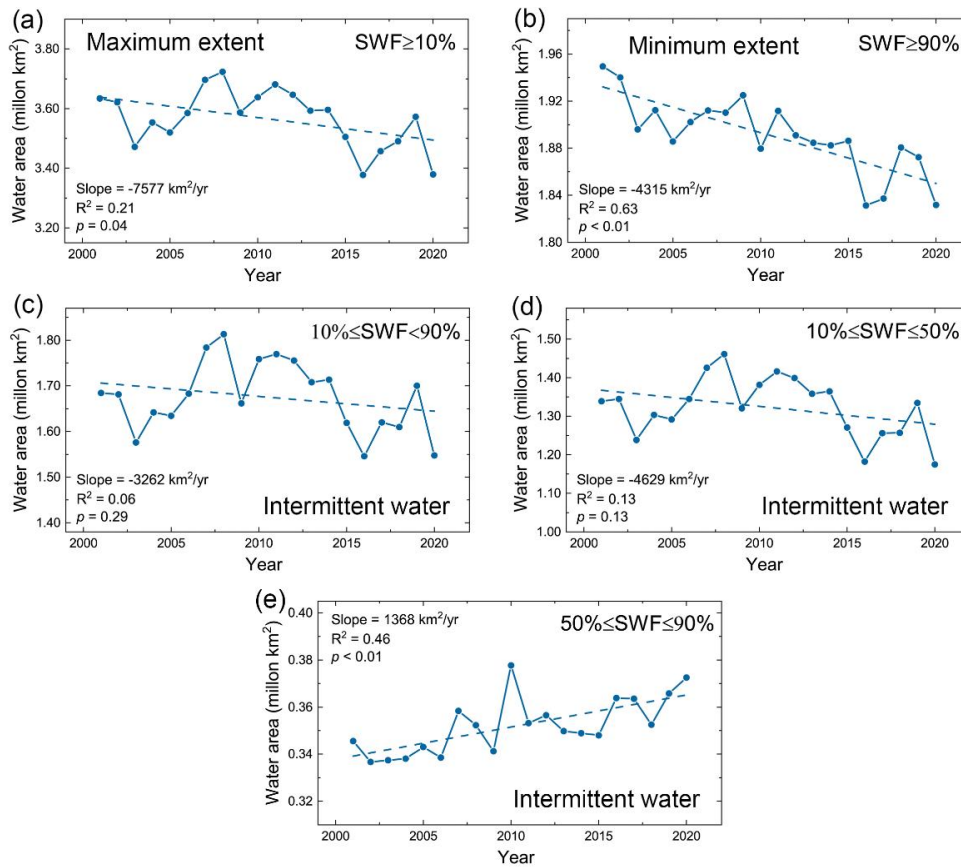
Figure 7. Interannual variation of the area of global surface water with different inundation frequency from 2001 to 2020. **(a)** Areas of the maximum surface water extent with SWF≥10%; **(b)** areas of the minimum surface water extent with SWF≥90%; Areas of the intermittent surface water extent with **(c)** 10%≤SWF<90%; **(d)** 10%≤SWF<50% and **(e)** 50%≤SWF<90%

A decreasing trend is observed for the area of global maximum and minimum surface water since 2001. The maximum water extent has been shrinking at a rate of -7577 km²/yr (p = 0.04) during 2001-2020, with the downward trend mainly occurred after 2012 (Fig. 7a). The area of permanent surface water has been decreasing continuously since 2001 at a rate of -4315 km²/yr (p < 0.01) (Fig. 7b). The intermittent surface water also shows an insignificant weak decreasing trend (-3262 km²/yr, p = 0.29). The intermittent surface water was divided up into two parts based on the value of SWF: intermittent water cover with 10% ≤ SWF < 50% and that with 50% ≤ SWF < 90%, and the areas were then calculated for these two types separately (Fig. 7d and 7e). The results show that the area of intermittent surface water with SWF less than 50% also showed a decreasing trend (-4629 km²/yr, p = 0.13) like the maximum water extent, indicating that the extent of global surface water in the wet season was shrinking. In contrast, an increasing trend is observed for the area of intermittent water with SWF above 50% (1368 km²/yr, p < 0.01), indicating that the temporal coverage period of some permanent water bodies was reduced, but still longer than half of a year.

Linear trend of SWF was mapped to demonstrate the monotonic changes of surface water inundation frequency during 2001-2020. For visualization, Tthe trend maps were aggregated to 10 km resolution for visualization. Figure 8 presents the and selected to display the fraction of positive slopes or negative slopes ($p < 0.05$), whichever is larger in each 10 km grid, to represent the main monotonic change type of surface water (Fig. 8a). percentage of pixels with significant positive and negative slopes ($p < 0.05$) as well as mean value of positive and negative slopes ($p < 0.05$) in each 10 × 10 km grid. Grids with dominantly positive (negative) slope were labeled as inundation frequency increasing (decreasing) areas (positive (negative) fraction). Similarly, we compared the average rate of positive slopes and negative slopes within each 10 km grid, and chose the faster change rate to represent the intensity of surface water changes (Fig. 8b). Grids with positive (negative) slope rate mean that the water occurrence is increasing (decreasing) rapidly. The results show notable changes of water cover extent in the high latitudes of the Northern Hemisphere. In the Arctic, there are more expanded lakes in the south, while the shrinking lakes are concentrated in the north, especially in the northern Arctic regions of Russia and Canada. This is consistent with the findings of Carroll Carrell et al. (2011) in Canada. The SWF has increased rapidly in the northern Tibetan Plateau at a rate of above 1.5%/yr (Fig. 8c), which is consistent with the observed extensive lake expansion and new lakes on the plateau due to increased glacial meltwater and precipitation (Zhang et al., 2017). Similar increase of SWF is also observed in southeastern Siberia, northern India, and northern central and northeastern parts of North America. In contrast, the inundation frequency has been mainly decreased for water bodies of Central Asia, Northern West Asia, Southeast Asia, southern China, as well as southern parts of South America.
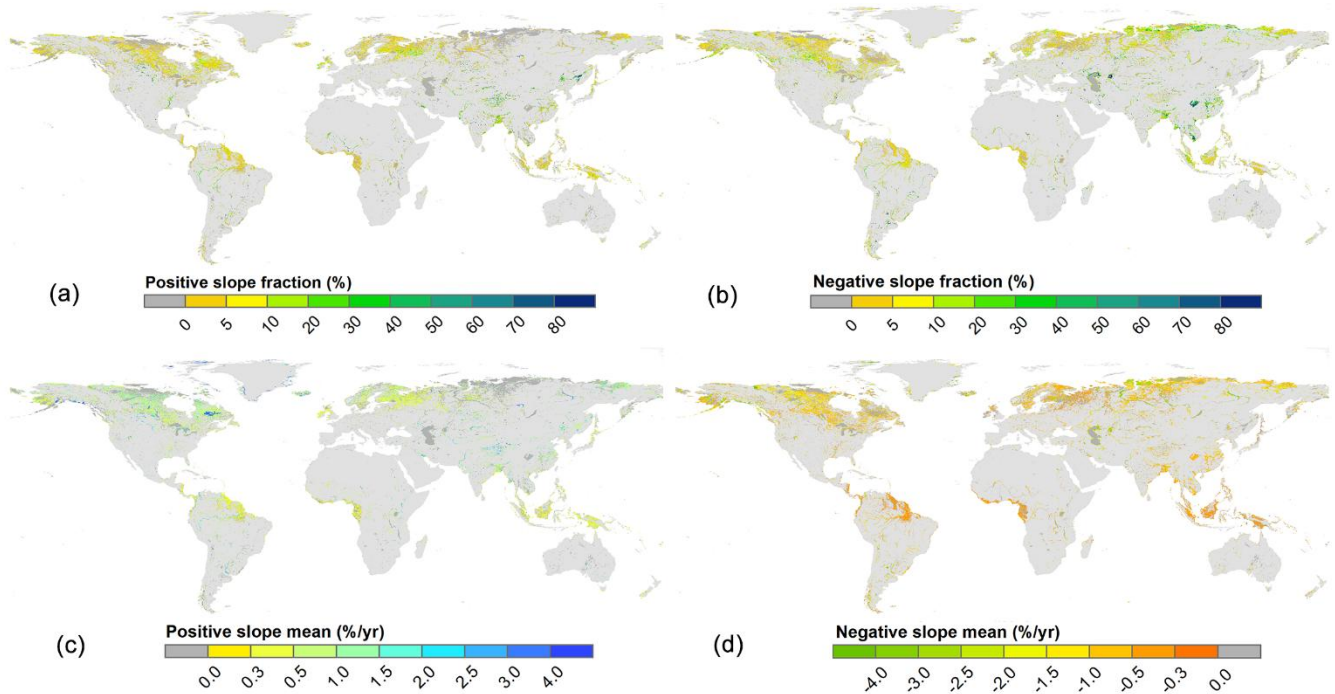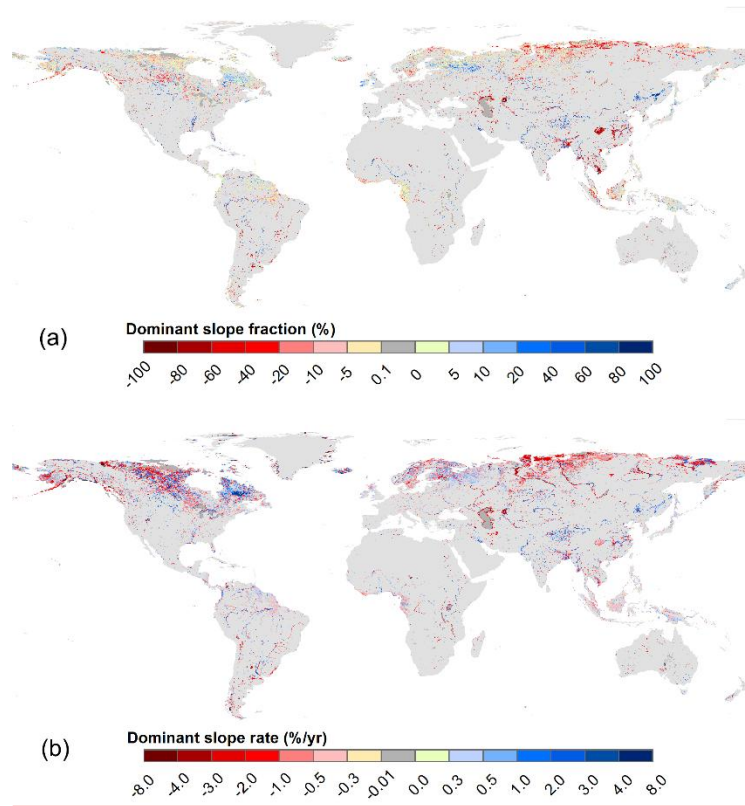
445

Figure 8. Linear trend of surface water cover frequency ~~(%/yr)~~ during 2001 and 2020. The trend maps were aggregated to 10 km resolution for visualization. ~~Percentage of pixels with~~ **(a)** Dominant SWF slope fraction (%). The positive (negative) fraction means that the fraction of pixels with increasing (decreasing) SWF ($p < 0.05$) in each 10 km grid, indicating whether the inundation frequency is dominantly increasing (decreasing).~~positive and~~ **(b)** Dominant SWF change rate (%/yr). The positive (negative) slope rate means that the mean linear slope rate of pixels with increasing (decreasing) SWF ($p < 0.05$) in each 10 km grid, whichever is faster, indicating whether the inundation frequency is increasing (decreasing) rapidly.~~negative slopes (p < 0.05) in each 10 × 10 km grid; Mean value of **(c)** positive and **(d)** negative slopes (p < 0.05) in each 10 × 10 km grid. The positive (negative) slope of Fig. 8c and 8d indicates whether the inundation frequency is increasing (decreasing).~~ The light grey refers to non-water covered areas.

4.5 Application examples for surface water dynamic analysis

455 Two examples are provided in this section to demonstrate the application of GLOBMAP SWF dataset in surface water dynamic analysis. These include the seasonal variation and interannual change of the Poyang Lake in southeastern China, and global top ten lakes with the largest seasonal dynamics.

4.5.1 Seasonal and interannual dynamics of Poyang Lake

Analysis of the seasonal and interannual dynamics of inland water body is illustrated in the Poyang Lake (28.28° N-29.89° N, 460 115.62° E-117.05° E), which is a large shallow lake located on the south bank of the middle and lower reaches of the

Yangtze River. It receives water from five rivers and the surrounding areas, and flows into the Yangtze River from the northern lake outlet. The lake shows significant seasonal variations of the water cover area due to the great seasonal fluctuations of regional precipitation and the runoff of the Yangtze River and the five rivers entering the lake, making it challenging to evaluate its interannual change. Figure 9a presents the spatial distribution of GLOBMAP SWF in 2020. The SWF value of most of the lake is ranging from 20% to 70%, indicating that the lake is mainly covered by intermittent water. The minimum lake area (SWF ≥ 90%) during the dry season of 2020 is 545 km^2, while the maximum area (SWF ≥ 10%) during the flood season reaches more than 7.4 times of the former (4062 km^2). Figure 9b shows the interannual series of water cover areas with different inundation frequencies. The maximum lake area shows remarkable fluctuation among years. The area of the maximum lake extent exceeded 4900 km^2 in 2002, 2010 and 2012; while it reduced to below 4000 km^2 in 2004, 2007, 2008, 2013-2015, 2017, and 2018; and the smallest area was only 3055 km^2 in 2011. The maximum lake area is closely related to the amount of water entering the lake during the flood season. The Poyang Lake Basin and the Yangtze River Basin are located in the East Asia monsoon region. The precipitation is mainly concentrated in summer and has significant interannual fluctuations, resulting in notable interannual variations of the lake area in the flood season. The interannual variation of lake area decreases gradually with the increase of SWF and reaches the lowest for the minimum lake extent that occurred during the dry season. Precipitation in the dry season (winter) is much fewer and less affected by abnormal climate, which may reduce the year-by-year fluctuation of the lake area in the dry season consequently. In 2003, the permanent lake area decreased abruptly from 947 km^2 to 512 km^2, and then remained at a low value with the area ranging from 500 km^2 to 660 km^2 for most years after 2003, which is coincided with the time of the impoundment of the Three Gorges Dam in 2003. These results are consistent with the decline of the annual minimum inundation area (Feng et al., 2012) and the rapid increase of wetland vegetation coverage in this region after 2002 (Han et al., 2015). The available clear-sky observations count was averaged over the maximum surface water extent in the Poyang Lake region for each year during 2001-2020 (purple line in Fig. 9b). The average N_{Clear} was between 33 and 39 during this 20-year period. Correlation was observed between the area of maximum surface water extent and the N_{Clear}. More clear-sky observations mean less precipitation, which may lead to smaller lake area. While less clear-sky observations mean more precipitation, and the lake area should be larger. However, the two variables do not correspond exactly, which indicates that the maximum surface water area does not depend on the available clear-sky observations number. The minimum surface water area shows no obvious correlation with N_{Clear}, and its interannual fluctuation should be related to precipitation and the amount of water entering the lake in the dry season.
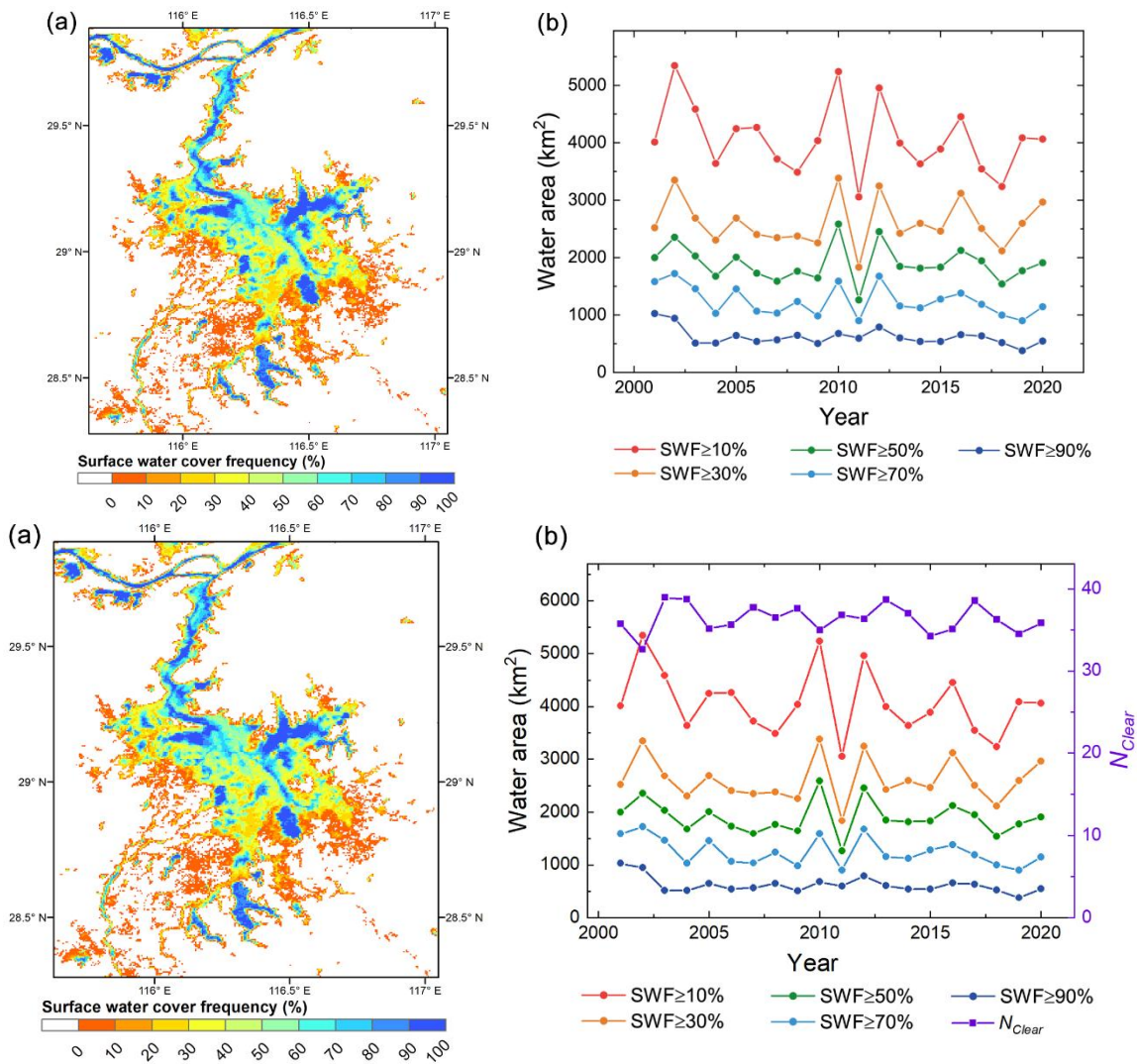
Figure 9. The seasonal variation and interannual change of surface water cover of Poyang Lake (28.28°N-29.89°N, 115.62°E-117.05°E). **(a)** The GLOBMAP SWF map in 2020; **(b)** The interannual variation of the area of Poyang Lake with different inundation frequency and average value of available clear-sky observations count (N_{clear}) over the maximum surface water extent from 2001 to 2020.

4.5.2 Top ten lakes with significant seasonal variation

The ten lakes with the largest seasonal variation in 2020 were identified to illustrate the seasonal fluctuation of inland open surface water. Seasonal variation was evaluated with the proportion ~~percentage~~ of the intermittent water area to~~in~~ the maximum water area in this year. All lakes whose maximum water cover extent > 3000 km^2 were ranked with their seasonal variation, and the top ten lakes were listed in Table 1.

The results show that the intermittent water area of these ten lakes accounts for more than 30% of the maximum water area. Poyang Lake in eastern China presents the largest seasonal fluctuation, with the seasonal variation reaching 84.29%. These ten lakes can be divided into three types: two natural freshwater lakes, four natural saltwater lakes and four reservoirs. Among them, natural freshwater lakes include Poyang Lake and Lake Peipus. Both lakes are shallow in depth, and the relief of the bottom and surrounding area are flat, which makes the water area may rise dramatically in flood season and fall during the dry season. For example, the shores of the Lake Peipus are usually flooded in the spring with the flooding area reaching up to 1000 km^2. Saltwater lakes include the Aral Sea, Lake Gairdner, Lake Eyre and Great Salt Lake. These lakes are all endorheic lakes that located in the arid regions of Central Asia, Australia and North America. Similar to the two freshwater lakes, the water depth is also shallow for these four saltwater lakes. In the wet season, the river runoff and local precipitation make the lake extent expand; while in the dry season, the lakes shrink significantly due to the strong evaporation. Four reservoirs, including Lake Kariba, Rybinsk Reservoir, La Grande River Reservoir and Lake Nasser, are also listed in the top ten lakes. The notable seasonal fluctuation of reservoir area should be related to artificial impoundment and drainage of the reservoir dam.

Table 1. Global top ten lakes with the largest seasonal variation in 2020.

Lake name	Country	Lake type	Maximum area (km^2)	Minimum area (km^2)	Intermittent water area (km^2)	Seasonal Variation (%)
Poyang Lake	China	Freshwater lake	3465.66	544.58	2921.08	84.29
Lake Kariba	Zambia, Zimbabwe	Reservoir	4558.92	1427.27	3131.66	68.69
Aral Sea	Uzbekistan, Kazakhstan	Saltwater lake	24188.81	9677.03	14511.79	59.99
Rybinsk Reservoir	Russia	Reservoir	4344.69	1761.92	2582.77	59.45
Lake Eyre	Australia	Saltwater lake	3870.94	1734.23	2136.71	55.20
Lake Gairdner	Australia	Saltwater lake	3958.95	1852.5	2106.45	53.21
La Grande River Reservoir	Canada	Reservoir	4626.11	2363.39	2262.72	48.91
Lake Eyre	Australia	Saltwater lake	3870.94	2230.09	1640.85	42.39
Lake Peipus	Estonia, Russia	Freshwater lake	3518.90	2069.95	1448.95	41.18
Great Salt Lake	America	Saltwater lake	7385.98	4446.01	2939.97	39.80
Lake Nasser	Egypt, Sudan	Reservoir	5033.32	3397.40	1635.91	32.50

5 Discussions

It is challenging to capture the interannual variation and change trend of inland water bodies due to their significant seasonal variations. The extent of surface water usually varies during a year due to the seasonal cycle of precipitation and evaporation, and it may also change abruptly due to large amount of rainfall and human activities, such as reservoir construction, mining, and irrigation (Tao et al., 2015). The timing of seasonal variation in surface water extent often varies among years due to

interannual shifts of the timing of precipitation and human activities. Thus, it may be incomparable for the snapshot of surface water acquired at the same period or during specific period such as the high-water period that is usually analyzed (e.g., in summer or wet season), which would misinterpret its interannual change and long-term trend. Here, we generated a global surface water cover frequency dataset from high-frequency MODIS data to characterize the seasonal variation and interannual change of inland water bodies. This dataset simplifies the multi-period water cover maps to the percentage of period that a pixel is covered by water in a year. It can characterize the temporal coverage frequency of surface water, which is suitable to represent the spatiotemporal characteristics of intermittent waters. The extent of maximum, minimum and different inundation frequency of surface water can be estimated from the dataset without the influence of the occurrence period, which helps to avoid misidentifying seasonal changes in water cover as interannual changes.

This paper developed a ~~novel~~ method for surface water extraction from a new perspective, which estimates the ~~surface water cover~~SWF indirectly by identifying land observations in annual observation series to reduce the influence of clouds, snow/ice and variable characteristics of water body and surface background. Water generally absorbs more solar radiation in spectral bands with longer wavelengths, resulting in the greater reflectivity of visible bands than that of NIR and SWIR bands. This spectral contrast has been widely used to extract surface water extent directly (e.g., GSWCD), and several spectral indices have been proposed for surface water extraction with the reflectance in the visible band (usually green) and NIR or SWIR band, such as Normalized Difference Water Index (NDWI) (McFeeters, 1996) and the Improved Normalized Difference Water Index (MNDWI) (Xu, 2006). To reduce the effects of clouds, the threshold of index is usually set to greater than zero in surface water mapping. When it comes to special water bodies with high reflectivities, such as frozen water, saline lake and turbid water bodies, the value of these indices may be below the threshold, resulting in miss detection. Additionally, variation of surface background may also result in confusion in water extraction, which has been demonstrated in the misdetection of lakes on the bright surface of northeastern Tibetan Plateau (Sect. 4.2). These may introduce substantial uncertainties in global water cover mapping with the direct water extraction algorithm. In generation of global water datasets, it is not only needed to propose good water cover extraction algorithm, but also need to consider data quality, noise and applicability of the algorithm in different regions. We found a reliable and robust method to separate land from water, cloud and snow/ice. The R_{Red} of the former is generally lower than that of R_{SWIR}, while it is opposite for the latter three. If the SWF were estimated indirectly by identifying land, the interference of cloud and snow/ice in water identification would be avoided. In this paper, instead of identifying water cover directly, the frequency of surface water cover was estimated by subtracting the land observations count from the total clear-sky observations count, which avoids directly distinguishing water from cloud and snow/ice. ~~Moreover, t~~The annual maximum water surface extent was extracted based on the minimum near-infrared reflectance composition method, which automatically excludes the influence of clouds, ice and snow. Moreover, the land identification method ($R_{Red} < R_{SWIR}$) was applicable for major types of water bodies and surface background, and can exclude cloud and snow/ice observations. Through these ~~two~~ procedures, the proposed algorithm ~~does not need to distinguish water from clouds and ice and snow, thus avoiding the possible confusion of the latter two on water detection. It is relatively easy to identify land observations since we do not need to distinguish between bright surface (such~~

as barren land and construction land) and dark surface (such as dense vegetation). The reflectivity of the red band of land is generally lower than that of the SWIR band, while it is opposite for water, cloud and snow/ice. This spectral feature is ubiquitous for various water bodies and surface background, and reduce the interference of cloud and snow/ice, which helps to improve the applicability of our algorithm for different regions across the globe.

Several factors may affect the performance of the proposed approach, including clouds, shadows, thawing of snow and ice, and spatial resolution. Clouds can obscure surface water signals in optical remote sensing. They usually occur more frequently during the rainy season, while the clear-sky observations are inclined to occur in the dry season. Since our algorithm uses the percentage of water observations in all clear-sky observations to estimate the water cover frequency within a whole year, the cloud observations that are concentrated in the rainy season are not taken into account, which may lead to underestimation of the SWF (Lake Mai-Ndombe in Fig. 6). The number of available clear-sky snow/ice-free observations in a year (N_{Clear}) was counted during the period 2001-2020 over global terrestrial surface. There are averagely 4,285 pixels with $N_{Clear} \leq 6$, accounting for 0.0008% of the total terrestrial surface pixels (550,215,315) in a year. This percentage is 0.02% (460 pixels out of total 1,901,338 water pixels) for the inland water bodies. Since the proportion of pixels with extreme sparse clear-sky observation is very small, its influences should be limited at global scale. Figure 10 shows the global map of N_{Clear} in 2020. Fortunately, N_{Clear} is generally above 40 in arid and semi-arid areas, where water bodies may show significant season variation in their extent. The low N_{Clear} values are concentrated in the tropics and subtropics, such as the Gulf of Guinea, the Amazon, the Southeast Asia, and the Sichuan Basin in southwestern China, where N_{Clear} is mostly ranging from 25 to 35. Since surface water generally shows relatively small seasonal changes in the tropics and subtropics, the available clear-sky observations should be able to capture the distribution of surface water. In high latitudes in the northern hemisphere, N_{Clear} is generally reduced to 10-25 due to long period of snow/ice cover and the polar night in winter. The proposed algorithm excludes snow/ice observations and uses the observations in unfrozen period to estimate the surface water cover frequency. In the glacial areas, such as Greenland and glacial areas of the Tibetan Plateau, N_{Clear} is less than 10 as snow and ice observations are excluded in counting of clear-sky observations, but it should have little impacts on the dataset due to limited water bodies in these regions. In some areas in the central part of several huge lakes (e.g., Caspian Sea), since they are far away from the land pixels on the shore and their clear-sky observations may be different from that of the adjacent reliable land pixels, N_{Clear} are set to fill value to reduce the uncertainties in N_{Clear} estimation. The SWF of these regions is usually estimated to be 100%, as its N_{land} is usually less than 15. The limited number of valid observations is a common problem for optical remote sensing. The MODIS onboard Terra and Aqua satellites observe the Earth's surface every 1 to 2 days. Their dense time series can be acquired to generate more clear-sky observations. Additionally, in the proposed method, all pixels with water count ≥ 3 among six observations with the lowest NIR reflectance were used to create the maximum surface water extent map. This means that the algorithm can be implemented with three valid observations during a year, which helps to improve the global applicability of the algorithm.
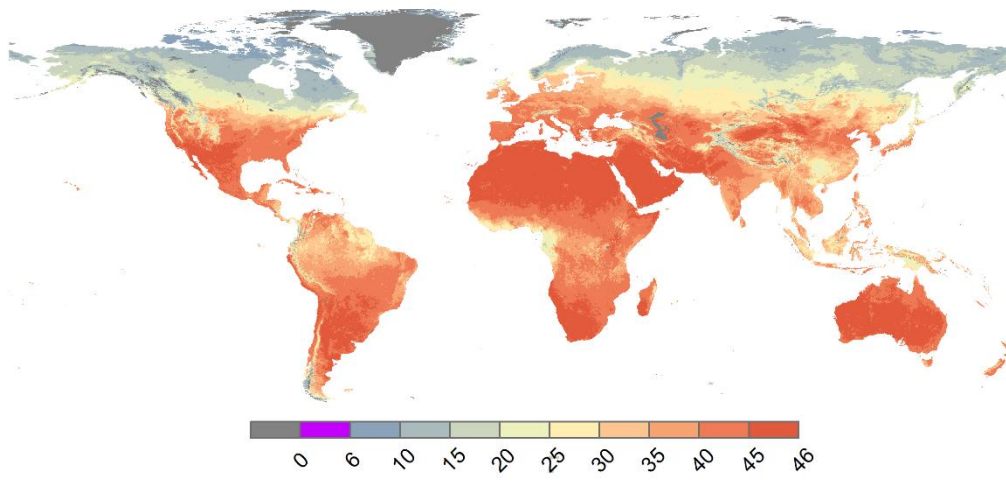
Figure 10. Global map of the number of clear-sky snow/ice-free MOD09A1 observation in 2020

The mountain shadows were masked using the criterion that the terrain slope derived from DEM data greater than 30º. In areas with complex terrain, this simplification may result in uncertainties of the estimation results. The variation of solar angle along latitudes and seasons was not considered in the slope criteria for shadows estimation, which may cause water that is outside of shadow to be removed in mountainous areas. Here, the DEM data was mainly used to exclude large areas mountain shadows, such as shadows in the margin of the Tibetan Plateau. For mountain shadows with a small range, since the local time when MODIS passes changes among days, the distribution of shadows will change due to different solar and viewing geometry. MOD09A1 selects the best possible observation during an 8-day composition period, and its spatial resolution is coarse (500 m), which help to reduce the effects of mountain shadows with a small range. It would help to improve the identification of terrain shadows by considering solar angle variation and using fine resolution DEM data, such as GMTED2010.

In snow/ice-covered areas, the meltwater on the ice would reduce the reflectivity in the NIR band. This may lead to overestimation of the maximum water area since the six observations with the lowest NIR reflectivity are used to extract the annual maximum water extent. Here, we create the maximum surface water extent map using those pixels with water count no less than 3 to remove possible false detections.

Additionally, the spatial resolution of MODIS may limit the identification for narrow rivers and small water bodies, resulting in underestimation of surface water extent. It is difficult for the dataset to capture small water bodies and the subtle changes of surface water, especially in high latitudes in the Northern Hemisphere where a large number of small water bodies are located. Satellite data often has certain advantages in terms of temporal or spatial resolution, time coverage, etc., but it is difficult to take into account all of these aspects. MODIS provides daily spectral measurements of the Earth surface since 2000. Its long-term high-frequency observations have unique advantages in monitoring of the seasonal and interannual

changes in surface water. High-resolution image such as Sentinel-1 and Sentinel-2 would help to improve the surface water extraction in these areas.

6 Data availability

The GLOBMAP SWF dataset is available on the Zenodo repository at https://doi.org/10.5281/zenodo.6462883 (Liu and Liu, 610 2022). The number of MOD09A1 clear-sky snow/ice-free observations (N_{Clear}) data is also provided as a quality dataset. The datasetIt is provided by 296 1200 km × 1200 km tiles at annual temporal and 500 m spatial resolutions in the sinusoidal projection with Geotiff format for each year during 2000-2020. The SWF file is named as "GLOBMAPSWF.AYYYY001.hHHvVV.V01.tif", while the N_{Clear} file is named as "GLOBMAPClearCount. AYYYY001.hHHvVV.V01.tif", where "YYYY" refers to the year of the file, and "HH" and "VV" explains the number of 615 tiles that are the same with MODIS standard tile. For the SWF dataset, Tthe valid range is 0-100, scale factor is 1.0, and unit is %. For the N_{Clear} dataset, the valid range is 0-46, scale factor is 1.0.

7 Conclusions

In this paper, a global annual surface water cover frequency dataset (GLOBMAP SWF) was generated at 500 m resolution from MODIS land surface reflectance data from 2000 to 2020. The SWF was proposed to quantitatively describe the 620 seasonal dynamics of inland water bodies by estimating the percentage of water cover occurrence in a year. The count of a pixel covered by water was estimated indirectly by subtracting the land observation count from total clear-sky observation count. The SWF was calculated by dividing the water count by the total number of clear-sky observations without the help of cloud mask.

In 2020, the area of global maximum surface water extent is 3.38 million km^2, of which the permanent surface water is 1.83 625 million km^2 (54%) and the intermittent surface water is 1.55 million km^2 (46%). The inland water bodies are mainly concentrated on mid-high latitudes of the Northern Hemisphere above 35° N. Compared with the high-frequent GSWCD and ISWDC datasets derived from MODIS data, the regional analysis demonstrates that our estimation results show better performances for frozen water and saline lake; the influence of clouds is successfully reduced, with the estimated SWF reaches 100% for permanent water bodies in cloud frequently covered regions; and the false detection was also reduced over 630 the bright surface in winter. When compared with the high-resolution GLAD and GSW datasets derived from Landsat data, the generated dataset captures more intermittent surface water, but small water bodies may be underestimated due to the coarse spatial resolution of MODIS. Our estimates are validated with the 10 m-resolution SWF maps extracted from Sentinel-1 SAR observations in four eight regions that covers lake, river and wetland. Consistent spatial pattern and good positive correlation are observed between the two results, with the R^2 up to 0.4683-0.97, RMSE ranging from 7.24% to 635 22.6211.28%, and MAE between 2.07% and 7.15%. During 2001-2020, a decreasing trend is observed for the area of global

maximum (-7577 km^2/yr, $p = 0.04$) and minimum (-4315 km^2/yr, $p < 0.01$) surface water. The intermittent water also showed an insignificant weak decreasing trend (-3262 km^2/yr, $p = 0.29$), while that with SWF above 50% has been expanding since 2001 (1368 km^2/yr, $p < 0.01$).

The GLOBMAP SWF dataset condenses the seasonal variation of inland water bodies to inundation frequency during a year.
640 It can characterize the spatial distribution of permanent water extent in the dry season and maximum water extent in the rainy season, as well as the distribution of intermittent water and the length of inundation period. The dataset can be used to analyze the interannual variation and change trend of surface water with consideration of its seasonal variation, and may guide the scientific management of water resources and the investment in water infrastructures.

645 **Author contributions.** LR designed the method, processed the MODIS data, and generated the surface water cover frequency dataset. LY analyzed and validated the dataset and wrote the manuscript. SR also analyzed and wrote the manuscript. All authors have read and approved the final paper.

Competing interests. The authors declare that they have no conflict of interest.
650

Acknowledgement. This research was funded in part by the Strategic Priority Research Program of the Chinese Academy of Sciences (XDA19080303); and in part by the Youth Innovation Promotion Association of Chinese Academy of Sciences (2019056); and in part by the Major Special Project-the China High-Resolution Earth Observation System (30-Y30F06-9003-20/22). The authors would like to thank the NASA Land Processes Distributed Active Archive Center for providing the
655 MODIS products.

References

Al Bitar, A., Parrens, M., Fatras, C., Luque, S. P., and Ieee: GLOBAL WEEKLY INLAND SURFACE WATER DYNAMICS FROM L-BAND MICROWAVE, IEEE International Geoscience and Remote Sensing Symposium (IGARSS), Electr Network, Sep 26-Oct 02, WOS:000664335304223, 5089-5092, 10.1109/igarss39084.2020.9324291, 2020.
660 Berghuijs, W. R., Woods, R. A., and Hrachowitz, M.: A precipitation shift from snow towards rain leads to a decrease in streamflow, Nat. Clim. Change, 4, 583-586, 10.1038/nclimate2246, 2014.
Bioresita, F., Puissant, A., Stumpf, A., and Malet, J. P.: A Method for Automatic and Rapid Mapping of Water Surfaces from Sentinel-1 Imagery, Remote Sens., 10, 10.3390/rs10020217, 2018.
Carroll, M. L., Townshend, J. R. G., DiMiceli, C. M., Loboda, T., and Sohlberg, R. A.: Shrinking lakes of the Arctic: Spatial
665 relationships and trajectory of change, Geophys. Res. Lett., 38, 10.1029/2011gl049427, 2011.

Chen, J., Chen, J., Liao, A. P., Cao, X., Chen, L. J., Chen, X. H., He, C. Y., Han, G., Peng, S., Lu, M., Zhang, W. W., Tong, X. H., and Mills, J.: Global land cover mapping at 30 m resolution: A POK-based operational approach, ISPRS J. Photogramm. Remote Sens., 103, 7-27, 10.1016/j.isprsjprs.2014.09.002, 2015.

Feng, M., Sexton, J. O., Channan, S., and Townshend, J. R.: A global, high-resolution (30-m) inland water body dataset for 2000: first results of a topographic-spectral classification algorithm, Int. J. Digit. Earth, 9, 113-133, 10.1080/17538947.2015.1026420, 2016.

Feng, L., Hu, C. M., Chen, X. L., Cai, X. B., Tian, L. Q., and Gan, W. X.: Assessment of inundation changes of Poyang Lake using MODIS observations between 2000 and 2010, Remote Sens. Environ., 121, 80-92, 10.1016/j.rse.2012.01.014, 2012.

Han, Q. Q. and Niu, Z. G.: Construction of the Long-Term Global Surface Water Extent Dataset Based on Water-NDVI Spatio-Temporal Parameter Set, Remote Sens., 12, 10.3390/rs12172675, 2020.

Han, X. X., Chen, X. L., and Feng, L.: Four decades of winter wetland changes in Poyang Lake based on Landsat observations between 1973 and 2013, Remote Sens. Environ., 156, 426-437, 10.1016/j.rse.2014.10.003, 2015.

Ji, L. Y., Gong, P., Wang, J., Shi, J. C., and Zhu, Z. L.: Construction of the 500-m Resolution Daily Global Surface Water Change Database (2001-2016), Water Resour. Res., 54, 10270-10292, 10.1029/2018wr023060, 2018.

Karlsson, J., Serikova, S., Vorobyev, S. N., Rocher-Ros, G., Denfeld, B., and Pokrovsky, O. S.: Carbon emission from Western Siberian inland waters, Nat. Commun., 12, 10.1038/s41467-021-21054-1, 2021.

Khandelwal, A., Karpatne, A., Marlier, M. E., Kim, J., Lettenmaier, D. P., and Kumar, V.: An approach for global monitoring of surface water extent variations in reservoirs using MODIS data, Remote Sens. Environ., 202, 113-128, 10.1016/j.rse.2017.05.039, 2017.

Klein, I., Gessner, U., Dietz, A. J., and Kuenzer, C.: Global WaterPack - A 250 m resolution dataset revealing the daily dynamics of global inland water bodies, Remote Sens. Environ., 198, 345-362, 10.1016/j.rse.2017.06.045, 2017.

Konapala, G., Mishra, A. K., Wada, Y., and Mann, M. E.: Climate change will affect global water availability through compounding changes in seasonal precipitation and evaporation, Nat. Commun., 11, 10.1038/s41467-020-16757-w, 2020.

Li, Y., Niu, Z. G., Xu, Z. Y., and Yan, X.: Construction of High Spatial-Temporal Water Body Dataset in China Based on Sentinel-1 Archives and GEE, Remote Sens., 12, 10.3390/rs12152413, 2020.

Li, Y., Zhao, G., Shah, D., Zhao, M. S., Sarkar, S., Devadiga, S., Zhao, B. J., Zhang, S., and Gao, H. L.: NASA's MODIS/VIIRS Global Water Reservoir Product Suite from Moderate Resolution Remote Sensing Data, Remote Sens., 13, 10.3390/rs13040565, 2021.

Liu, J. Y., Kuang, W. H., Zhang, Z. X., Xu, X. L., Qin, Y. W., Ning, J., Zhou, W. C., Zhang, S. W., Li, R. D., Yan, C. Z., Wu, S. X., Shi, X. Z., Jiang, N., Yu, D. S., Pan, X. Z., and Chi, W. F.: Spatiotemporal characteristics, patterns, and causes of land-use changes in China since the late 1980s, J. Geogr. Sci., 24, 195-210, 10.1007/s11442-014-1082-6, 2014.

Liu, R. G. and Liu, Y.: GLOBMAP SWF: a global annual surface water cover frequency dataset since 2000 for change analysis of inland water bodies (Version 1.0), Zenodo [data set], https://doi.org/10.5281/zenodo.6462883, 2022.

700 Lu, S. L., Ma, J., Ma, X. Q., Tang, H. L., Zhao, H. L., and Baig, M. H. A.: Time series of the Inland Surface Water Dataset in China (ISWDC) for 2000-2016 derived from MODIS archives, Earth Syst. Sci. Data, 11, 1099-1108, 10.5194/essd-11-1099-2019, 2019.

Liao, A. P., Chen, L. J., Chen, J., He, C. Y., Cao, X., Chen, J., Peng, S., Sun, F. D., and Gong, P.: High-resolution remote sensing mapping of global land water, Sci. China Earth Sci., 57, 2305-2316, 10.1007/s11430-014-4918-0, 2014.

705 Lutz, A. F., Immerzeel, W. W., Shrestha, A. B., and Bierkens, M. F. P.: Consistent increase in High Asia's runoff due to increasing glacier melt and precipitation, Nat. Clim. Change, 4, 587-592, 10.1038/nclimate2237, 2014.

McFeeters, S. K.: The use of the normalized difference water index (NDWI) in the delineation of open water features, Int. J. Remote Sens., 17, 1425-1432, 10.1080/01431169608948714, 1996.

Miara, A., Macknick, J. E., Vorosmarty, C. J., Tidwell, V. C., Newmark, R., and Fekete, B.: Climate and water resource
710 change impacts and adaptation potential for US power supply, Nat. Clim. Change, 7, 793-+, 10.1038/nclimate3417, 2017.

Otsu, N. A.: Threshold Selection Method from Gray-Level Histograms, IEEE Trans. Syst. Man Cybern., 9 (1), 62-66, 1979.

Papa, F., Prigent, C., Aires, F., Jimenez, C., Rossow, W. B., and Matthews, E.: Interannual variability of surface water extent at the global scale, 1993-2004, J. Geophys. Res. Atmos., 115, 10.1029/2009jd012674, 2010.

Padron, R. S., Gudmundsson, L., Decharme, B., Ducharne, A., Lawrence, D. M., Mao, J. F., Peano, D., Krinner, G., Kim, H.,
715 and Seneviratne, S. I.: Observed changes in dry-season water availability attributed to human-induced climate change, Nat. Geosci., 13, 477-+, 10.1038/s41561-020-0594-1, 2020.

Pekel, J. F., Cottam, A., Gorelick, N., and Belward, A. S.: High-resolution mapping of global surface water and its long-term changes, Nature, 540, 418-+, 10.1038/nature20584, 2016.

Pickens, A. H., Hansen, M. C., Hancher, M., Stehman, S. V., Tyukavina, A., Potapov, P., Marroquin, B., and Sherani, Z.:
720 Mapping and sampling to characterize global inland water dynamics from 1999 to 2018 with full Landsat time-series, Remote Sens. Environ., 243, 10.1016/j.rse.2020.111792, 2020.

Prigent, C., Papa, F., Aires, F., Rossow, W. B., and Matthews, E.: Global inundation dynamics inferred from multiple satellite observations, 1993-2000, J. Geophys. Res. Atmos., 112, 10.1029/2006jd007847, 2007.

Prigent, C., Jimenez, C., and Bousquet, P.: Satellite-Derived Global Surface Water Extent and Dynamics over the Last 25
725 Years (GIEMS-2), J. Geophys. Res. Atmos., 125, 10.1029/2019jd030711, 2020.

Ran, L. S., Butman, D. E., Battin, T. J., Yang, X. K., Tian, M. Y., Duvert, C., Hartmann, J., Geeraert, N., and Liu, S. D.: Substantial decrease in CO_2 emissions from Chinese inland waters due to global change, Nat. Commun., 12, 10.1038/s41467-021-21926-6, 2021.

Tao, S. L., Fang, J. Y., Zhao, X., Zhao, S. Q., Shen, H. H., Hu, H. F., Tang, Z. Y., Wang, Z. H., and Guo, Q. H.: Rapid loss
730 of lakes on the Mongolian Plateau, Proc. Natl. Acad. Sci. U.S.A., 112, 2281-2286, 10.1073/pnas.1411748112, 2015.

Tortini, R., Noujdina, N., Yeo, S., Ricko, M., Birkett, C. M., Khandelwal, A., Kumar, V., Marlier, M. E., and Lettenmaier, D. P.: Satellite-based remote sensing data set of global surface water storage change from 1992 to 2018, Earth Syst. Sci. Data, 12, 1141-1151, 10.5194/essd-12-1141-2020, 2020.

Vermote, E.: MOD09A1 MODIS/Terra Surface Reflectance 8-Day L3 Global 500m SIN Grid V006 [data set], distributed by

735   NASA EOSDIS Land Processes DAAC, https://doi.org/10.5067/MODIS/MOD09A1.006, 2015.

Xu, H. Q.: Modification of normalised difference water index (NDWI) to enhance open water features in remotely sensed imagery, Int. J. Remote Sens., 27, 3025-3033, 10.1080/01431160600589179, 2006.

Yamazaki, D., Trigg, M. A., and Ikeshima, D.: Development of a global similar to 90 m water body map using multi-temporal Landsat images, Remote Sens. Environ., 171, 337-351, 10.1016/j.rse.2015.10.014, 2015.

740   Zhang, G. Q., Yao, T. D., Piao, S. L., Bolch, T., Xie, H. J., Chen, D. L., Gao, Y. H., O'Reilly, C. M., Shum, C. K., Yang, K., Yi, S., Lei, Y. B., Wang, W. C., He, Y., Shang, K., Yang, X. K., and Zhang, H. B.: Extensive and drastically different alpine lake changes on Asia's high plateaus during the past four decades, Geophys. Res. Lett., 44, 252-260, 10.1002/2016gl072033, 2017.

Zhang, G. Q., Yao, T. D., Chen, W. F., Zheng, G. X., Shum, C. K., Yang, K., Piao, S. L., Sheng, Y. W., Yi, S., Li, J. L.,

745   O'Reilly, C. M., Qi, S. H., Shen, S. S. P., Zhang, H. B., and Jia, Y. Y.: Regional differences of lake evolution across China during 1960s-2015 and its natural and anthropogenic causes, Remote Sens. Environ., 221, 386-404, 10.1016/j.rse.2018.11.038, 2019.